Spin waves in 3d metals:
a Resonant Inelastic X-Ray Scattering study of epitaxially grown thin films

Master's Degree in Engineering Physics
Academic year 2019-2020

Candidate **Filippo Elgorni** *919214*

Supervisor **Giacomo C. Ghiringhelli**
Co-supervisor **Nicholas B. Brookes**

Abstract

This Thesis focuses on spin waves in ferromagnetic 3d transition metals. These collective excitations of a ferromagnetic ground state have been studied for years by Inelastic neutron Scattering (INS), able to measure their dispersion quite directly. Here we focus on the possibility to address their study with Inelastic X-Ray Scattering (RIXS), a newer technique that has been rarely employed in the study metallic systems.

All the experimental work was carried out at the ID32 beamline of the European Synchrotron Radiatoin Facility (ESRF) in Grenoble, France. Here, a high resolution, state of the art, RIXS spectrometer has been used to measure two ferromagnetic systems: fcc cobalt and fcc nickel in the form of thin film single crystals, epitaxially grown and characterized *in situ*.

The results are positive as they show that RIXS is capable of measuring spin wave dispersions even for metals, which is still debatable at the current time, even for materials that are typically inaccessible by INS, namely nanometric thin films. Fcc cobalt data shows good agreement with neutron studies of comparable alloy systems, but still displays some discrepancies with *ab initio* calculations. Fcc nickel is instead more problematic: the acquired spectra show degradation effects after long measurement times, that lead to an anomalous shift in the dispersion. The importance of the magnetization direction for RIXS measurements is also considered and taken into account.

This work highlights the possibility of using RIXS as a complementary technique for the study of collective excitations, namely spin waves, also in metals. This opens the possibility of reliably measuring other systems that are unaccessible to INS, although some aspects of the technique are still to be mastered.

Estratto

Questa Tesi si concentra sulle onde di spin nei metalli di transizione 3d ferromagnetici. Queste eccitazioni collettive dello stato fondamentale ferromagnetico sono state studiate per anni con lo Scattering Anelastico di Neutroni (INS), in grado di misurare la loro dispersione in maniera diretta. Qui ci concentriamo sulla possibilità di affrontare il loro studio con lo Scattering Anelastico di Raggi X (RIXS), una tecnica più recente raramente impiegata nello studio sistemi metallici.

Tutto il lavoro sperimentale è stato svolto presso la beamline ID32 dell' Struttura Europea di Radiazione di Sincrotrone (ESRF) a Grenoble, Francia. Qui, uno spettrometro RIXS ad alta risoluzione è stato utilizzato per misurare due sistemi ferromagnetici: cobalto cfc e nichel cfc nella forma di film sottili a cristallo singolo, cresciuti epitassialmente e caratterizzati in situ.

I risultati sono positivi e dimostrano che RIXS è in grado di misurare le dispersioni delle onde di spin anche per i metalli, possibilità ad oggi ancora discussa, anche per materiali che sono tipicamente inaccessibili ad INS, come film sottili nanometrici. I dati sul cobalto cfc sono compatibili con studi a neutroni di leghe simili al sistema in esame, ma mostrano ancora alcune discrepanze con i calcoli ab initio. *Il nichel cfc è invece più problematico: gli spettri acquisiti mostrano effetti di degradazione causati dai lunghi tempi di misura, che portano ad uno spostamento anomalo della dispersione. Per quest'ultimo caso, si sottolinea l'importanza della direzione di magnetizzazione per le misure RIXS.*

Questo lavoro evidenzia la possibilità di utilizzare RIXS come tecnica complementare per lo studio delle eccitazioni collettive, in particolare delle onde di spin, anche nei metalli. Questo apre la possibilità di misurare in modo affidabile altri sistemi che non sono accessibili ad INS, nonostante alcuni aspetti della tecnica siano ancora da padroneggiare.

Contents

List of Figures

List of Tables

Chapter 1

Introduction

The study of magnetism is a strongly established field of research that extends its domains from the fundamental understanding of physical phenomena to the developement of novel applications [1]. Among various systems, often complicated and exotic, elementary 3d metals, studied exceedingly in their electronic and magnetic properties, still lack a proper description in many details surrounding their static and dynamic magnetic behaviour. They are in principle simple, but their non-local nature and the strong correlation effects play an important role that make detailed predictions hard to make [1, 2, 3].

The field of Itinerant Ferromagnetism, that tries to tackle this many-body problem, usually relies on calculations, and still needs strong experimental comparisons especially for what concerns dynamical phenomena. Spin waves, collective excitations of a ferromagnetic ground state, are one of these. Although they have been discussed since the 1930s, their description in metals, mostly in terms of *ab initio* calculations, is still lacking good predictive capabilities [2, 4].

Historically, the fundamental technique for their experimental study has been Inelastic Neutron Scattering (INS) with which they were first measured in ferrite in 1957 [5]. In the next 40 years, the technique has developed strongly, becoming more and more consolidated [6]: INS has little limitation on the type of probed material, and has successfully characterized the spin wave dispersion of insulators (see for example refs. [7, 8]) and metals, like the ones we'll cover in this work (see refs. [9, 10, 11, 12, 13]). The main limitation of this powerful technique is the need of fairly big samples, with weights in the order of grams [6].

Recently, Resonant Inelastic X-Ray Scattering (RIXS), a relatively new technique that probes many of the elementary excitations of solids [14] (charge density waves, d-d, excitons, plasmons and phonons) was shown to be successful in the measurement of spin waves as well [15, 16, 17]. The European Synchrotron Radiation Facility (ESRF) is currently the first hard x-ray fourth generation synchrotron light source in the world [18] and its soft-RIXS beamline, ID32, the result of many years of upgrades [19, 20], already delivered important and competitive results in the field [21]. For what concerns spin waves, one of the differences with INS is the possibility of working with much smaller samples, even of nanometric scale, opening the possibility of studying materials which are produced by physical and chemical methods and that are impossible to grow up to the sizes needed for INS.

Althogh many novel systems have been successfully probed, with particular interest in the field of high T_C superconductors, Mott insulators and other strongly correlated materials, little work has been done for RIXS on metals. This is possibly due to the presence of a high fluorescence background that covers up interesting regions in the spectrum of the emitted

photons. However, recent work from both ID32 at ESRF [22], where the experiments of this Thesis have also taken place, and from the Brookhaven National Laboratory [23], clearly show that RIXS can be used to probe excitations in metals as well, particularly spin waves. As it had happened with strongly correlated systems, this puts RIXS in the position of being an alternative, or more precisely a complementary technique, to Inelastic Neutron Scattering and Spin Polarized Electron Energy Loss Spectroscopy (SPEELS).

In the following work we address RIXS spectroscopy of 3d metals with the precise aim of probing spin waves. The 3d ferromagnetic metals are iron, cobalt and nickel: the former was studied successfully and in depth in the references above [22, 23], showing good agreement with previous data from INS and with theoretical *ab initio* calculations [24], which slightly underestimate the dispersion energies. Nickel instead, studied again by the same group of ID32, showed an unexpected energy deviation with respect to both, which is discussed in section 2.2. The starting point for this work is then to go back to nickel and try to determine the nature of the previous effect, trying to understand if the dispersion flattening is of physical nature or has to do with effects of the technique.

This behaviour, along with the difference between measures and theory, which generally overestimates the energies even with respect to INS, was ascribed to correlation effects, which are known to be stronger in nickel than in iron. To check this hypothesis as well, a new system was taken into consideration and was studied in the second part of this work: fcc cobalt. This material, which is not stable in bulk at standard conditions (where it is usually hcp), is obtained with epitaxial growth and can be seen as an in-between case to the former two in terms of electronic and magnetic structure. If correlations have any effect on the dispersion, their intermediate appearance should be observed in this system as well.

Epitaxial growth is chosen for samples of both materials, that are measured mostly in the $[0\sqrt{21}]$ direction. It shall be noted that this low symmetry direction was chosen by accident, and due an error done in the characterization phase, where a LEED diffraction pattern was interpreted with an offset of 45°. The initial measures where intended for the [111] direction, but since the spin wave dispersion is more or less isotropic (as will be discussed in chapter 2 and appendix A) it was difficult to recognize the error. Some measurements are also performed in the [001] direction, inspired by the work of ref. [23].

A more solid understanding of dynamic spin phenomena in metallic media, as the one presented in this work, could be helpful in different ways.

First of all, having good knowledge of spin waves in elementary systems, supported by experiments of different nature, is the starting point for developing stronger *ab initio* computational methods. Many calculations are still too far from reproducing the real systems, and providing more experimental data is key to highlight the right direction, for example in terms of the chosen approximations. When this will be done, the possibility could be that of eventually engineer materials, in this case metallic alloys, with wanted properties in a computationally optimized way [3].

More generally, spin waves are showing an increasing relevance and the phenomenon lacks some details in its understanding [2]. The work at ESRF, together with that of Brookhaven, hints to results that are in acceptable agreement with other techniques. If INS and SPEELS results are replicated to a good extent, RIXS could be then considered as a complementary technique for the field. Moreover, this could open new possibilities for the study of systems that are partially different to those measured by the other two, as RIXS probes both bulk like behaviour, at variance with the surface sensitivity of SPEELS, and for much smaller samples than the ones of INS. Epitaxially grown films display a huge variety of possibilities that can

be taken into account and that are simply inaccessible to INS: small samples, multilayers, thermodynamically unstable phases and so on. To a certain extent, the study of fcc cobalt presented in this work already applies this idea.

Lastly, the work presented hereafter also tries to broaden the scope of RIXS as a whole. The focus of the technique has been historically bound to strongly correlated systems: cuprates [25, 17, 21], nickelates [26, 27], functional oxides [28] and iridates, all of which are insulators or semiconductors. The possibility to probe, characterize and explore metallic samples, with the advantages of above, might broaden the reach of this new spectroscopy technique. The results of this work and those of refs. [22, 23] shall be taken as first steps in this potentially new direction.

Chapter 2

Spin Waves

Spin waves, often referred to as magnons in quasiparticle language, are collective excitations in spin ordering of a ferromagnetic material.

They have been part of the discussion on the magnetic properties of solids for almost a century: while the spontaneous magnetization of ferromagnets is well described by Curie-Weiss law and renormalization group theory close to critical point ($M(T)/M(0) \propto (T - T_C)^{\beta}$, where β is the wilsonian critical exponent [1]), a proper description for the low temperature empirical relation

$$M(T)/M(0) = 1 - \left(\frac{T}{\Theta}\right)^{\frac{3}{2}} \tag{2.1}$$

was already found by Bloch in 1930 [29] by including low energy perturbations of spin ordering that follow a quadratic dispersion [1]. In the equation, which is now referred to as Bloch's Law, Θ is nothing but a constant while $M(0)$ is the magnetization of the system at 0 K.

In the following years, much work has been done both in the experimental and theoretical directions, as welle as for different systems. Spin waves can be described in a semiclassical manner, where they appear as a collective precession of spins around their position (fig. 2.1), or in a full quantum-dynamical fashion, where they are taken as a superposition of spin flips from the ground state.

In this chapter, we first describe a simple model where spins are completely localized, and obtain an analytical spin wave dispersion relation $E(\mathbf{q})$. We then complete the picture with more recent developments, particularly those concerning the differences that arise when a metallic media, whose electrons have a delocalized nature, is taken into account. This will be done together with some information on the computational approaches that are fundamental to the topic.

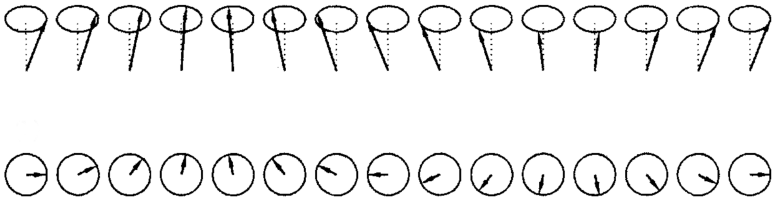

Figure 2.1: Semiclassical representation of a 1D spin wave. Adapted from [1].

Understanding the nature of spin waves in metallic media bears on a more general understanding of magnetism in metals. Moreover, as it will be made clear later, it is the best way to verify how much computational tools are reliable for eventual material search and compound engineering in the near future.

2.1 Local Theory of Spin Waves

In the following section we present a simple derivation of spin waves, where they emerge as elementary excitations of a ferromagnetic ground state.

All of what follows is based on the assumption that we are describing atoms on a regular lattice of j sites, where the exchange integral J completely dominates over all magnetic effects. For the moment, we are completely neglecting the metallic nature of our sample: we ignore this issue, as it will be covered in the next section.

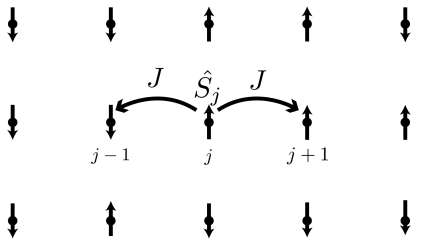

Figure 2.2: Schematic depiction of the system described in this section.

The spin operator for each atomic site is $\hat{S}_j$, with its related ladder operators S_j^+ and S_j^- defined as usual (see for example ref. [1]). We perform a transformation introduced by Holstein and Primakoff in 1940 [30] that maps the spin operators onto bosonic creation and annihilation operators $\hat{b_j^\dagger}$ and $\hat{b_j}$. This can be done as it can be shown that all spin commutation rules are preserved.

$$\begin{aligned}
\hat{S}_j^z &= S - \hat{n}_j \\
\hat{S}_j^+ &= \sqrt{2S - \hat{n}_j}\hat{b}_j \approx \hat{b}_j\sqrt{2S} \\
\hat{S}_j^- &= \hat{b}_j^\dagger\sqrt{2S - \hat{n}_j} \approx \hat{b}_j^\dagger\sqrt{2S}
\end{aligned} \tag{2.2}$$

It is clear that in this mapping the vacuum state is the one in which all sites have positive $+S$ spin along the z axis. In eq. (2.2) we have also expanded the spin ladder operators linearly: this approximation is especially good at low temperatures, where the number of excitations $\hat{n}_j$ in the ground state is small. We then take the Heisenberg Hamiltonian:

$$\begin{aligned}
H &= -J\sum_{\langle i,j\rangle}\hat{\mathbf{S}}_i\cdot\hat{\mathbf{S}}_j = \\
&= -J\sum_{\langle i,j\rangle}[\hat{S}_i^z\hat{S}_j^z + \frac{1}{2}(\hat{S}_i^+\hat{S}_j^- + \hat{S}_i^-\hat{S}_j^+)]
\end{aligned} \tag{2.3}$$

and substitute each term in its approximate form. Here $\langle i,j\rangle$ means that the sum is performed over nearest neighbours. After some algebra, the result can be written as:

$$\begin{aligned}
H &= -\frac{NZ_0JS^2}{2} + JS\sum_{\langle i,j\rangle}(\hat{b}_i^\dagger - \hat{b}_j^\dagger)(\hat{b}_i - \hat{b}_j) \\
&= E_0 - \frac{JS}{2}\sum_i\sum_{\mathbf{a}}(\hat{b}_i^\dagger\hat{b}_{i+\mathbf{a}} + \hat{b}_{i+\mathbf{a}}^\dagger\hat{b}_i) + JSZ_0\sum_i\hat{n}_i
\end{aligned} \tag{2.4}$$

Z_0 is the coordination number, and N the number of atoms in the system. The first term, that we choose to call E_0, is the energy of the ground state in which all spins point in the same direction, while the remaining part is the energy of excitations in the lattice. The approximation made in eq. (2.2) is what limits the accuracy of eq. (2.4): higher order approximations would have delivered higher order terms, as for example magnon-magnon interactions. The summing over nearest neighbours is made explicit by the use of the lattice vector $\mathbf{a}$, pointing to the Z_0 atoms, and by a factor $1/2$ accounting for double counting. The bosonic operators can be represented in momentum space:

$$\begin{aligned} \hat{b}_j^\dagger &= \frac{1}{\sqrt{N}} \sum_{\mathbf{q}} e^{-i\mathbf{q}\cdot\mathbf{r}_j} \hat{b}_{\mathbf{q}}^\dagger \\ \hat{b}_j &= \frac{1}{\sqrt{N}} \sum_{\mathbf{q}} e^{i\mathbf{q}\cdot\mathbf{r}_j} \hat{b}_{\mathbf{q}} \end{aligned} \tag{2.5}$$

leading to:

$$\begin{aligned} H &= E_0 + Z_0 JS \sum_{\mathbf{q}} \left[1 - \frac{1}{Z_0} \sum_{\mathbf{a}} \cos(\mathbf{q}\cdot\mathbf{a}) \right] \hat{b}_{\mathbf{q}}^\dagger \hat{b}_{\mathbf{q}} \\ &= E_0 + \sum_{\mathbf{q}} E(\mathbf{q}) \hat{n}_{\mathbf{q}} \end{aligned} \tag{2.6}$$

where of course $\hat{b}_{\mathbf{q}}^\dagger \hat{b}_{\mathbf{q}} = \hat{n}_{\mathbf{q}}$ can be interpreted as the number operator of the spin excitations at momentum $\mathbf{q}$, which will be of bosonic nature and with unitary spin [31]. These take several names: "magnon" follows the usual quasiparticle jargon, while "spin wave" is more reminiscent of their intuitive meaning.

It is interesting to give an analytical expression of the dispersion $E(\mathbf{q})$ for given directions. The reason is that energy dispersions are what is primarily measured in experiments, at the same time containing information on some parameters of the system. For example, measuring the dispersion of spin waves gives numerical information on the product JS. The final shape of the curve depends on the lattice (the set of nearest neighbour vectors $\mathbf{a}$) and on the direction of $\mathbf{q}$, which is an experiment parameter.

In what follows we quickly specialize eq. (2.6) to the case of our experiment. All measurements were on fcc crystals, a lattice with coordination number $Z_0 = 12$ and atoms positioned as in fig. 2.3. Measures were taken along the [001] and [0$\sqrt{}$21] directions, so we take a look at $E(q)$ along these.

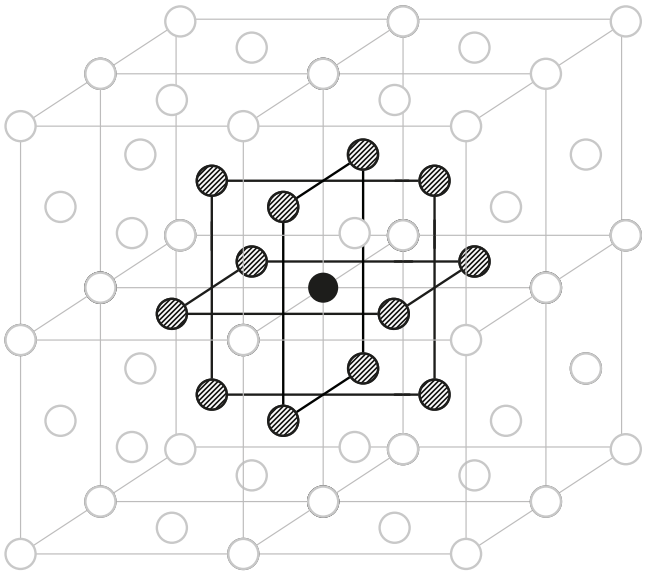

Figure 2.3: Fcc lattice. For a given atom, its twelve nearest neighbours are shown.

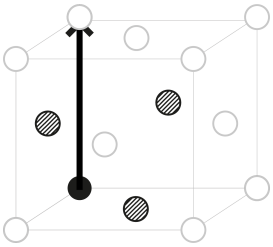

(a) The [001] direction.

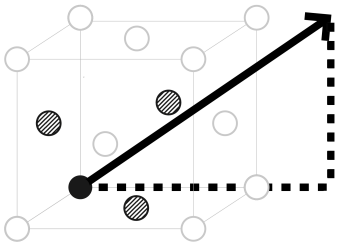

(b) The [0$\sqrt{}$21] direction.

Figure 2.4: The two directions of propagation for the measured spin waves.

Starting with the [001] direction, we can see that four of the total twelve vectors give null vector product inside a cosine, and the other eight are $\cos(qa/2)$, where a is the lattice constant of the fcc lattice (see fig. 2.4a).

$$\begin{aligned} E(q) &= 12JS\left[1-\frac{1}{12}\left(4+8\cos\frac{qa}{2}\right)\right] \\ &= 8JS\left(1-\cos\frac{qa}{2}\right) \end{aligned} \tag{2.7}$$

For the [0$\sqrt{}$21] direction things get quickly more complicated. The dispersion reduces to:

$$E(q) = 12JS\left[1-\frac{1}{3}\left(\cos\frac{qa}{\sqrt{12}}+\cos\frac{qa}{\sqrt{6}}+\cos\frac{qa}{\sqrt{12}}\cos\frac{qa}{\sqrt{6}}\right)\right] \tag{2.8}$$

The two dispersions have a different range in q, but peculiarly enough reduce to the exact same at high wavelengths. If we take the limit of small q in fact we can use $\cos x \approx 1 - x^2/2$:

$$E(q) \approx 8JS\left(1 - 1 + \frac{1}{2}\frac{q^2a^2}{4}\right) = Dq^2$$
$$E(q) \approx 12JS\left(1 - 1 + \frac{1}{3}\frac{q^2a^2}{4}\right) = Dq^2 \tag{2.9}$$

Notice that we have defined $D = JSa^2$ in the same way for both dispersions. This parameter is usually referred to as "Spin Wave Stiffness Constant" [2, 32] and is the main parameter obtained by dispersion measures. It can be shown quite effortlessly that the result obtained for these two directions is in fact general for all $\mathbf{q}$ in the fcc lattice and for any cubic lattice (see appendix A). D can then be regarded as a property of the material.

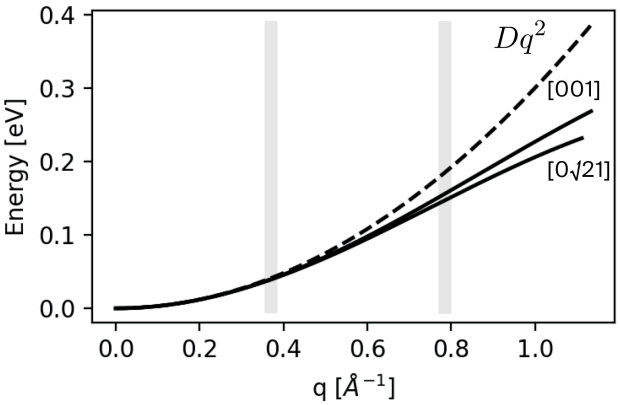

Figure 2.5: The dispersions for the two directions and their long wavelength approximation. The gray bars roughly delimit the region of our measurements.

Each spin wave is a delocalized excitation with unitary spin: they will increase with temperature decreasing the magnetization from its saturation value $M(0)$. We can evaluate their number considering the density of states $\rho(\omega) \propto \sqrt{\omega}$ for a quadratic dispersion:

$$n_{magnon} = \int_0^\infty \frac{\rho(\omega)d\omega}{e^{\beta\hbar\omega} - 1} \propto \left(\frac{T}{D}\right)^{\frac{3}{2}} \tag{2.10}$$

where $\beta = 1/k_BT$ with k_B the Boltzmann constant. This result is Bloch's law as soon as we realise that $M(0) - M(T) \propto n_{magnon}$. The name "stiffness" now finds justification for its meaning, as D dictates how hard it is to get away from saturation magnetization by just raising temperature.

2.2 Spin Waves in Metals

In the previous section we have seen a straightforward derivation of spin waves, which gave an analytical expression for their dispersion that is isotropic at long wavelengths. Although little

approximation was made (always justified by the low temperature limit), we have to recall the initial premise of dealing with a lattice of localized spins. While the model is rather accurate for insulators and materials in which electrons are bound to their relative atoms, we must remember that our systems of interest are ferromagnetic transition metals. Here electrons are delocalized and the magnetic moment assumes fractional value, so their wave nature must be taken into account. It is then legitimate to take some care adapting the previous results.

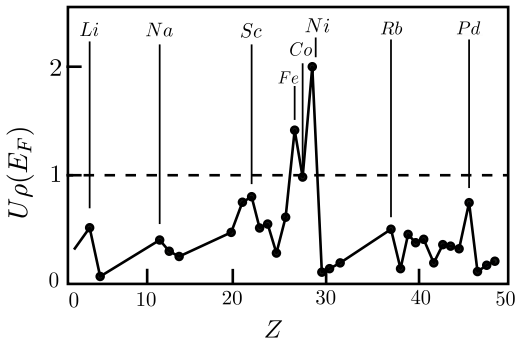

Figure 2.6: The Stoner criterion for some metals. Adapted from [3]

The framework under which magnetic effects are treated in metals is usually referred to as "Itinerant Magnetism" (or "Band Magnetism"), and can be seen as an extension of electron band theory inclusive of magnetic and exchange interactions [1, 3]. It should be remarked that, apart from the apparent simplicity of the problem, many aspects remain unsolved and impossible to address without the aid of numerical methods and experiments.

Non-ferromagnetic effects in metals are described under some degree by Pauli paramagnetism and Landau-Peierls diamagnetism, while a ferromagnetic approach was developed by Slater and Stoner and later formalized as a mean field decoupling of the Hubbard model [1]. The main result is that, given a material, if the equation $U\rho(E_F) \geq 1$ is satisfied (U is the onsite strength of the electron repulsion) then ferromagnetism must take place. This criterion finds great agreement between calculations (where U is evaluated numerically [3]) and the fact that only three 3d transition metals are known to be ferromagnets: iron, cobalt and nickel. The model is however too simple to include other effects: among the discrepancies the low temperature magnetization obtained in the Stoner framework $M(T) - M(0) \propto T^2$ is in contrast with experiments, where a Bloch-like behaviour is also observed [2]. The difference in exponent should then presumably hint to spin waves of the same nature as the ones from the previous section.

In their 1951 and 1952 papers [33, 34] Herring and Kittel were among the first to address this point. Along with a theoretical model that tries to account for the presence of spin waves in ferromagnetic metals, one concern is to provide general arguments on why their presence should be generally accepted and their dispersion quadratic, regardless of the media or theoretical model.

One of the problems of modelling spin waves in metallic media is the presence of the "Stoner continuum" [1, 35]. This region of the momentum-energy plane is one where spin excitations from one spin-split band to the other can take place. As shown pictorially in fig. 2.7, there is a precise region in which this region and the spin wave dispersion interact. Usually, what is thought is that inside the region the spin wave dispersion is still present, but damped (meaning excitations also appear in its neighbouring areas), a concept that is referred to as "Landau Damping" [2]. A clear description of what happens is still missing, and disagreement between experiments and *ab initio* calculation is still present.

As anticipated, a more effective way to treat the many body problem from a theoretical point of view is by doing so with the aid of computers. In fact, most of contemporary literature on the topic focuses on building models and expanding approximations that can provide good simulations of what is seen experimentally. In some cases, the theoretical justifications at the

base of calculations can hint analytically to our previous eq. (2.6) as for example in ref. [36]. Throughout the years different approaches to the problem and different approximations have been used to calculate compete spin wave dispersions, with more or less good agreement with data. Giving a detailed outlook on all such implementations is out of the scope of this work, but a schematic and chronological introduction can be found in ref. [2].

Density Functional Theory (DFT) methods are nowadays a standard choice for *ab initio* calculations of quantum systems of many kinds. These must be adapted in the perspective of dealing with magnetic phenomena, with the conventional electron density replaced by spin density. The most difficult part is then having to deal with exchange correlation effects: these are usually taken care of by a family of approximations that go under the name of Local Spin Density Approximation (LSDA). In "Theory of Itinerant Electron Magnetism" by Kübler [3] a proper definition of LSDA is given, along with different applications to the whole field of magnetic metals. One of such is obtaining a computable dispersion for spin waves, which finds good agreement with data.

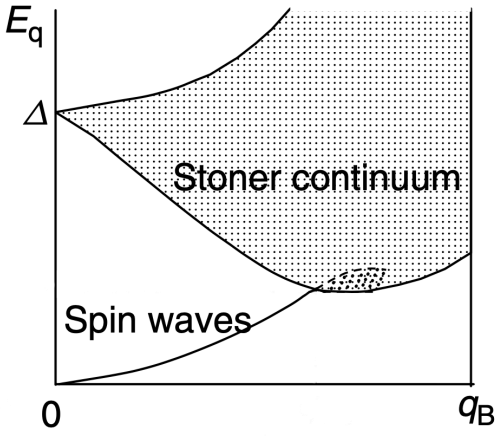

Figure 2.7: The stoner continuum and its crossing with the spin wave dispersion for a strong itinerant ferromagnet like nickel and cobalt. Δ is the exchange splitting between the bands and q_B is the wavevector at the Brillouin boundary. Adapted from [35].

LSDA however finds difficulties at finite temperatures. A different framework is given by Melnikov in the book "Dynamic Spin Fluctuation Theory of Metallic Magnetism" [2]. Here magnetism in metals is treated from a rather general point of view, with the study of the susceptibility matrix χ and its dynamics. Spin waves are treated, together with Stoner excitations and all magnetic effects, on the same level.

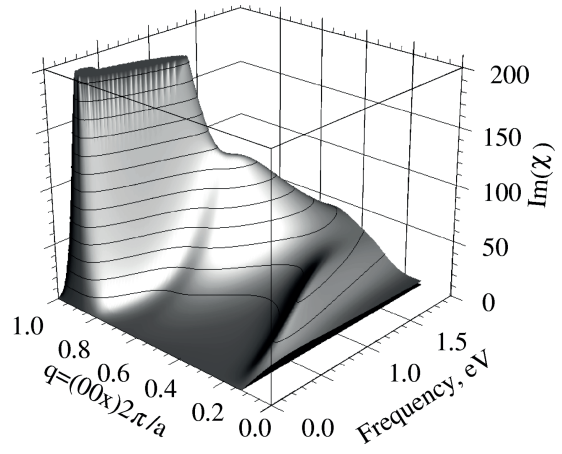

Figure 2.8: An example result from a DSFT calculation. The peak position for each q can be seen as a dispersing, but more information is present in the manifold shape.Taken from [2]

In the book it is shown that the imaginary part of the matrix χ is what is measured in experiments: the treatment in the book gives meaning to transverse components of such matrix by applying the Random Phase Approximation (RPA) and identifies both spin waves and Stoner excitations in its singularities. This work presents a computational approach that is at the basis of the most recent calculations, which goes under the name of Dynamical Spin Fluctation Theory (DSFT). The output of such calculations is not only a dispersion, but more generally a manifold, as $\chi = \chi(\omega, \mathbf{q})$ is function of both momentum and energy. This gives the possibility of quantitatively comparing experiments also in the domain of peak shape, and not only in position. In this case, the anticipated difficulty in modelling the interaction between the spin wave dispersion and the Stoner con-

tinuum is surpassed by a modelling of both: the expected effects should for example be visible as a damping of spin wave intensity when the Stoner region is accessed [2].

The importance of an experimental comparison is key to evaluate the reliability of available numerical methods. The experimental data is not used to complete the free parameters in given models, but it's rather compared with *ab initio* calculations. This process helps understanding which of the available approximations gives the more consistent result, in order to assume their validity in more general cases. It is hoped that, in the future, the computational approaches developed thanks to this back-and-forth process will be enough to help designing and engineering new materials with desired properties [3, 2].

Chapter 3

Resonant Inelastic X-Ray Scattering

In this chapter we briefly introduce Resonant Inelastic X- Ray Scattering spectroscopy, both its theoretical basis, its applications for measuring collective excitations, and its implementation in the spectrometer present at the ID32 beamline of the European Synchrotron Radiation Facility.

We will start with a description of the scattering process itself and will try to point out how excitations can be seen. Then, we will briefly take a look at the instrument configuration present at ID32. Finally, magnetic excitations observed by RIXS are summerised along with some of the relevant works in this area. A more complete and in depth treatment is given for instance by Ament et al. [14].

3.1 General theory of the RIXS process

Resonant Inelastic X-Ray Scattering (RIXS) is a "photon-in, photon-out" *Scattering* process involving *X-Rays*. It is *Inelastic* as energy is generally not conserved: the lower energy of the outgoing photons is absorbed, among other channels, by collective excitations of the material. If these are described as common with their associated quasiparticles (phonons, excitons and, in our case, magnons) we are allowed to use the simple conservation rules:

$$\begin{aligned} \hbar\mathbf{k} &= \hbar\mathbf{k}' + \hbar\mathbf{q} \\ \hbar\omega_{\mathbf{k}} &= \hbar\omega_{\mathbf{k}'} + E_{\mathbf{q}} \end{aligned} \tag{3.1}$$

where $\mathbf{k}$ ($\mathbf{k}'$) and $\omega_{\mathbf{k}}$ ($\omega_{\mathbf{k}'}$) are momentum and frequency of the incoming (outgoing) photon, while $\mathbf{q}$ and $E_{\mathbf{q}}$ are the momentum and energy of the quasiparticle excitation in the material.

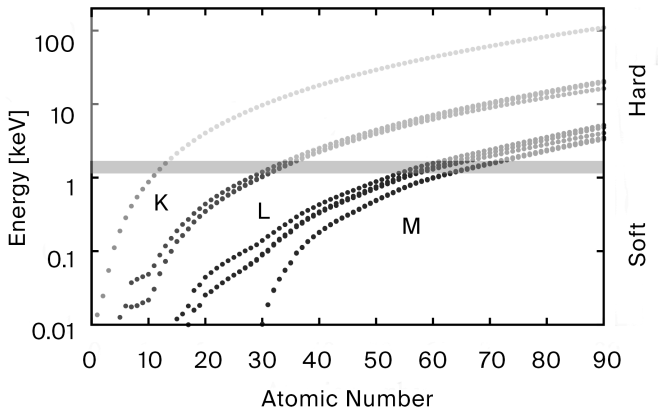

Figure 3.1: K, L and M edges in function of atomic number. The soft X-ray regime is highlighted. Adapted from [37].

An important feature of the technique, and of the process, is that it is *Resonant*. Differently from other techniques RIXS is based on a second order scattering process. One consequence of this, that we will explain soon in more detail, is that the scattering process needs to be at resonance with an electronic transition in order to be visible. The incoming photons must then be tuned in frequency to trigger particular transitions of the probed sample, usually those from deep lying energetic states to outer bands. These are referred to as edges, and are specific of each element. This gives the possibility of performing a chemical tuning as choosing one or another edge gives the possibility to observe the contributions of electrons from various elements in the sample. It is also this that justifies the use of X-ray synchrotron radiation, as these transitions lie in a wide range of energies. In this work we'll focus on soft RIXS, with energies between 400-1600 eV, as this energy regime is the one implemented at ID32, where our experiments have been carried out. As it can be seen in fig. 3.1, the energy range is enough to cover the K edges of nitrogen and oxygen, the M edges of rare earths and, to our interest, the L edges of 3d transition metals.

A pictorial way to look at the process is as in fig. 3.2. An electron is promoted from a deep core state to an outer band by absorbing a photon. The intermediate state $|n\rangle$ is virtual, and the modification of the system with the introduction of the hole can let another electron relax with an extra excitation of the material while a second photon is emitted. Scattering to this state could be enhanced by the resonant process, resulting in a peak in the spectra.

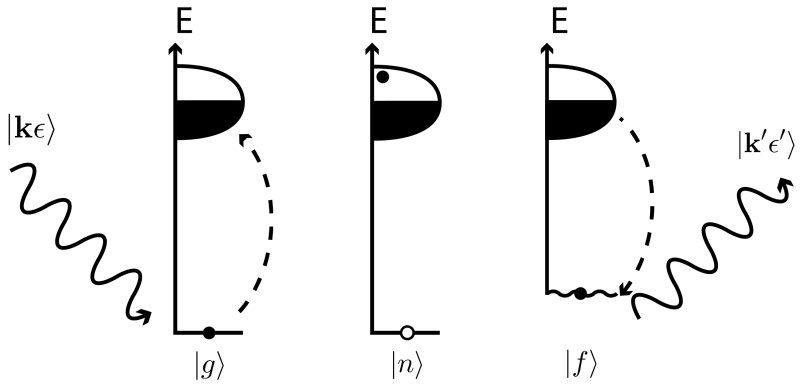

Figure 3.2: Three steps of the RIXS process. In the end, a collective excitation in the material, like spin waves, is depicted by the wiggle.

To give an analytical description of the scattering process we consider a transition triggered by photon-matter interaction.

We take the Hamiltonian describing the whole system (both the electrons in the solid and the electromagnetic field) and split it in two terms as follows: $H = H_0 + H'$.
The first one, H_0, affects both electrons and photons, but separately. It is the part that defines the eigenstates of the system, and thus those that are the initial ("ground") and final states of our scattering problem. As they act on (yet) uncoupled degrees of freedom we can simply write:

$$\begin{aligned} |\mathtt{g}\rangle &= |g\rangle \otimes |\mathbf{k}\epsilon\rangle = |g; \mathbf{k}\epsilon\rangle \\ |\mathtt{f}\rangle &= |f\rangle \otimes |\mathbf{k}'\epsilon'\rangle = |f; \mathbf{k}'\epsilon'\rangle \end{aligned} \tag{3.2}$$

where we obviously have that for instance $|g\rangle$ is the initial state of the solid, while $|\mathbf{k}\epsilon\rangle$ is the state of the incoming photon (labelled by wavevector $\mathbf{k}$ and polarization ϵ).

The second part of the Hamiltonian, H', is the one that only includes the coupling of matter with the electromagnetic field, and is treated as a perturbation. It is this one that can be "switched on" during the interaction. Then, the typical way to treat state transitions in a quantum mechanical formalism is by doing so with the help of Fermi's Golden Rule. The transition rate w is:

$$w = \frac{2\pi}{\hbar} \sum_{\mathtt{f}} \left| \langle \mathtt{f}| \, H' \, |\mathtt{g}\rangle + \sum_n \frac{\langle \mathtt{f}| \, H' \, |n\rangle \, \langle n| \, H' \, |\mathtt{g}\rangle}{E_\mathtt{g} - E_n} \right|^2 \delta(E_\mathtt{f} - E_\mathtt{g}). \tag{3.3}$$

Here, in contrast with plenty of textbook examples, the second order terms is also included. It can be immediately seen that although usually negligible, it becomes more and more prominent when the denominator gets close to zero: $E_\mathtt{g} - E_n = E_g + \hbar\omega_\mathbf{k} - E_n \approx 0$. This is satisfied when the photon energy is in resonance with a transition from electron ground state to a virtual state $|n\rangle$. As previously anticipated, we choose to tune our incoming photons to a specific edge of an element in our system. It must be stressed that the state $|n\rangle$ is only virtual, thus physically intermediate to the whole process. In the final state $|\mathtt{f}\rangle$ some electron will surely have relaxed back to fill the hole in the original core state as the highly excited state is also unstable; the solid in itself however could have gained some excitation in the form of collective motion. Intuitively, if energy can be transferred to excitations in some preferential way, we will see a peak for that one channel.

Proceeding with our analytical treatment, the equation would require us to use a complete description of light-matter interaction. This is properly done by quantum electrodynamics, although in an unfeasible manner. Fortunately, the scale of energies participating in a condensed matter system is usually well below the relativistic limit, and an approximate interaction Hamiltonian can be expressed as follows:

$$\begin{aligned} H' = \sum_{i=1}^{N} \Big[\frac{e}{m} \mathbf{A}(\mathbf{r}_i) \cdot \mathbf{p}_i + \frac{e^2}{2m} A^2(\mathbf{r}_i) + \frac{e\hbar}{2m} \sigma_i \cdot \nabla \times \mathbf{A}(\mathbf{r}_i) + \\ - \frac{e^2\hbar}{(2mc)^2} \sigma_i \cdot \frac{\partial \mathbf{A}(\mathbf{r}_i)}{\partial t} \times \mathbf{A}(\mathbf{r}_i) \Big] \end{aligned} \tag{3.4}$$

Here the vector potential is intended in its usual second-quantized form (see for example ref. [38]). We completely neglect the first terms of the transition rate in eq. (3.3), as we know from experiments that the second one dominates in resonant scattering. Here, only the first and third terms (of non-magnetic and magnetic nature) of eq. (3.4) give nonzero amplitudes. It can be shown that the magnetic terms is of much smaller intensity: we have essentially discarded all but one interaction terms in H' and we can write

$$\frac{e^2\hbar}{2m^2V\epsilon_0\sqrt{\omega_k\omega_{k'}}}\sum_n\sum_{i,j=1}^{N}\frac{\langle f|\, e^{-i\mathbf{k}'\cdot\mathbf{r}_i}\epsilon^{*\prime}\cdot\mathbf{p}_i\,|n\rangle\,\langle n|\, e^{-i\mathbf{k}\cdot\mathbf{r}_j}\epsilon\cdot\mathbf{p}_j\,|g\rangle}{E_g+\hbar\omega_k-E_n+i\Gamma}=$$

$$=\frac{e^2\hbar\sqrt{\omega_k\omega_{k'}}}{2V\epsilon_0}\sum_n\frac{\langle f|\,\mathcal{D}'^{\dagger}\,|n\rangle\,\langle n|\,\mathcal{D}\,|g\rangle}{E_g+\hbar\omega_k-E_n+i\Gamma}=$$

$$=\frac{e^2\hbar\sqrt{\omega_k\omega_{k'}}}{2V\epsilon_0}\mathcal{F}_{fg} \tag{3.5}$$

To simplify the notation we have introduced the transition operator $\mathcal{D}$ and the scattering amplitude $\mathcal{F}_{fg}$. The lifetime broadening Γ is also introduced to account for all the other relaxation channels. The transition rate w can be then related to the double-differential cross section obtaining the principal equation describing the RIXS process:

$$\frac{d^2\sigma}{d(\hbar w)d\Omega}=\frac{e^4\omega_{k'}^3\omega_k}{16\pi^2\epsilon_0^2c^4}\sum_f|\mathcal{F}_{fg}|^2\,\delta(E_g-E_f+\hbar\omega) \tag{3.6}$$

which is known as the Kramers-Heisenberg equation. A finite temperature version of this equation can be derived as well, but it is omitted as all our measures were carried out at T = 20K.

In its simplified form of eq. (3.6), it might seem hard to understand how RIXS can give knowledge on the probed material. One has to remember that the sought information is contained in the $|f\rangle$ states: the probability to access one is proportional to $\mathcal{F}_{fg}$, and thus depends on the transitions *to* and *from* the intermediate states $|n\rangle$. The set of eigenstates of the hamiltonian H_0, which includes the effects of the core hole on the remaining electrons, takes then part in the scattering amplitude. It is not granted that every quasiparticle, spin waves being no exception, is actually seen in the process.

3.2 Overview of the RIXS spectrometer at ID32

We have seen that RIXS is a second order scattering process, which means it is inherently photon-hungry. Moreover, it needs a properly tunable source of X-rays, with a wide enough range of frequencies to cover the edges of different elements of interest. At the moment only synchrotron radiation satisfies both demands, ensuring high brilliance [39] and resolution in all the X-ray band. RIXS is a highly specialised technique, performed only in a few laboratories in the world, with increasing demand due to the novelty of its measurements [40]. In the following section we review the basic information on the instrument used to perform the measures of this work.

3.2.1 Synchrotron radiation

Although they have given essential contribution to material science and biology, X-rays have undergone very few changes in their production technique: from their discovery in 1895 until almost a century later the main device has been the X-ray tube. When the first circular accelerators started to be used for the study of subatomic physics, a new idea for producing high quality X-rays emerged, and with it the first synchrotron light sources.

The concept is to use radiation emitted by accelerated charged particles, namely electrons or more rarely positrons, that are kept rotating at relativistic speed and constant energy in what is called a "storage ring", a toroidal vacuum tube. Intuitively, it is the centripetal force, provided by bending magnets, that lets electrons emit tangentially to their trajectory. Although this also true, in reality X-ray emission is mostly taken care of by undulators. These devices are linear arrays of dipoole magnets with alternating polarity: the resulting sinusoidal magnetic field generates a coherent movement of the relativistic electrons. X-ray emission is much more controlled: the light is no longer white, but it is centered around a frequency of choice with a somewhat narrower band. The band can be tuned by operating mechanically on the undulator piece. Moreover, the emitted beam has intrinsic higher brilliance than the one produced by the bending magnets. It is these segments, which are alternated with the curved ones of the ring, that produce the X-rays that are actually used in experiments. Each couple of elements is associated to a laboratory, called "beamline" from the geometry of the tangential beam, that uses X-rays produced in its own undulator (see fig. 3.4). Monochromatic light is finally obtained from the narrow band with the aid of monochromators [39].

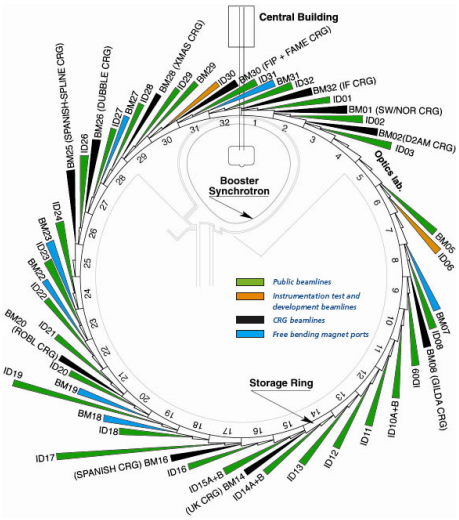

Figure 3.3: Schematic of the ESRF storage ring with its beamlines. Taken from [41].

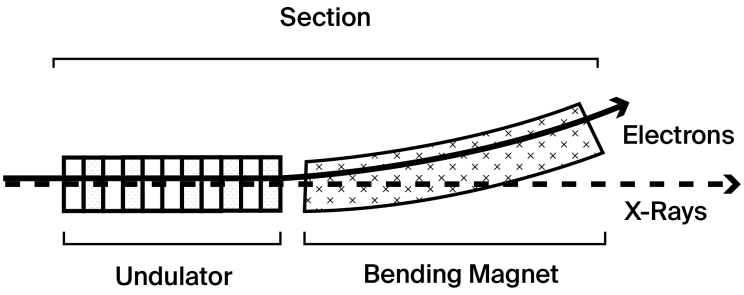

Figure 3.4: A schematic representation of a synchrotron section. Each undualtor belongs to a specific beamline.

Nowadays, latest generation synchrotrons reach a brilliance which is of 12 orders of magnitude above the one of X-ray tubes. The improved overall quality of X-ray beams has given the field a completely new range of scopes, and the number of possible uses is growing.

All the experiments of this work have been carried out at the European Synchrotron Radiation Facility, a joint project of 22 countries situated in the scientific polygon of Grenoble, France. It officially started its activity in September 1994 and currently counts 40 beamlines tangential

to the storage ring, with a diameter of 844m. From August 2020 the Extremely Bright Source (EBS) project completed its first step [18]. This upgrade let ESRF increase its brightness by a factor of 100 with respect to its previous stage, making it the first 4th-generation high energy synchrotron light source of the world. ESRF operates at 6 GeV and up to 200 mA current, with refills scheduled for approximately every hour [42].

3.2.2 ID32 Beamline

ID32 is an upgrade beamline at ESRF specialized in soft X-ray scattering and absorption spectroscopy. It opened officially in 2014 as a direct evolution of ID08, and is currently one of the few beamlines which are external to the old experimental hall. The beam is produced with two APPLE-II undulators [43] and travels to the two endstations, at 110m and 120m respectively from the ring. The undulators ensure a range of energies from 400 eV to 1600 eV, with total freedom in the choice of polarization (either vertical, horizontal, or circular). The monochromator is implemented with a plane mirror and four variable line spaced (VLS) gratings: the former is of dedicated design, it is cross shaped and liquid nitrogen cooled to ensure thermal stability, while the gratings are all of different spacing.

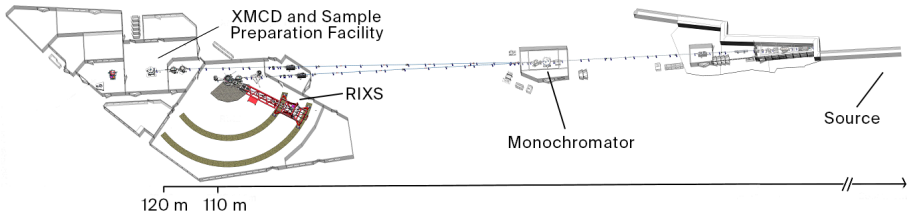

Figure 3.5: Top view of the beamline layout. Adapted from [41].

The beamline presents two branches: the beam can be directed to either of the two with the use of a deflecting mirror just after the monochromator. The first branch is for polarization dependent X-Ray Absorption Spectroscopy, and is in direct contact with a Sample Preparation Facility, while the second only includes the RIXS spectrometer. As most of the information of the absorption branch is contained in the following chapter (section 4.1 and section 4.2 for what concerns sample preparation, section 4.1.3 for what concerns X-Ray Absorption Spectroscopy), we only focus on the RIXS branch in what follows [19].

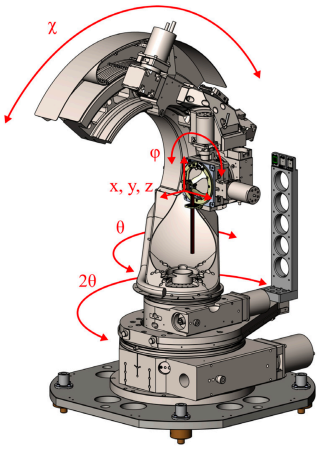

Figure 3.6: The RIXS four circle goniometer. Taken from [19].

High resolution RIXS is a fairly new technique: the instrument at ID32 has been one of the first in its kind, and introduced many technical innovations with respect to previous generation machines (AXES at ID08 and SAXES at the ADRESS beamline at the Swiss Light Source [44, 45, 20]). Its optical scheme, schematized in fig. 3.7, is however quite simple to describe [19]. The spectrometer makes use of a four circle goniometer to hold the sample, see fig. 3.6. This allows to move it freely to desired positions: incoming and outgoing X-rays define the the scattering plane, which is intended to be horizontal. Beam characterization is performed with a razor blade that can be mounted on the same sample slot. Cooling is also ensured by liquid helium to a minimum of circa 17K. The outgoing beam is then horizontally collimated until it reaches a spherical VLS grating that

disperses the X-ray energies in the vertical direction. These beams then access a vacuum tube of around 10 meters at the end of which a CCD detector is installed. To ensure the possibility of choosing the direction (and thus wavevector) of scattered X-rays, all the elements from collimator to detector must be able to move freely. Vertical and longitudinal motion are performed mechanically quite easilly. The arm has a 100° range of horizontal rotation which is allowed without breaking vacuum from the sample chamber: this lets the spectrometer perform dispersion measurements with decreased times and complete automation. Although it is not the case of this work, a polarimeter and a second CCD detector allow polarization-dependent measurements [19].

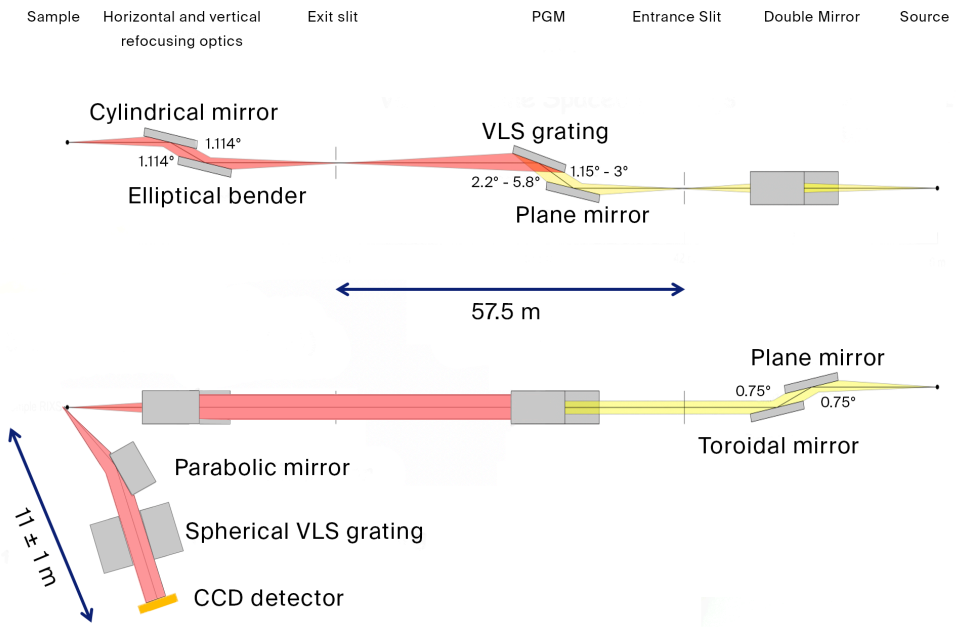

Figure 3.7: Side and top view of the RIXS spectrometer optical layout. Adapted from [41].

Figure 3.8: The sample chamber and the analyser of the RIXS spectrometer at ID32. Taken from [41].

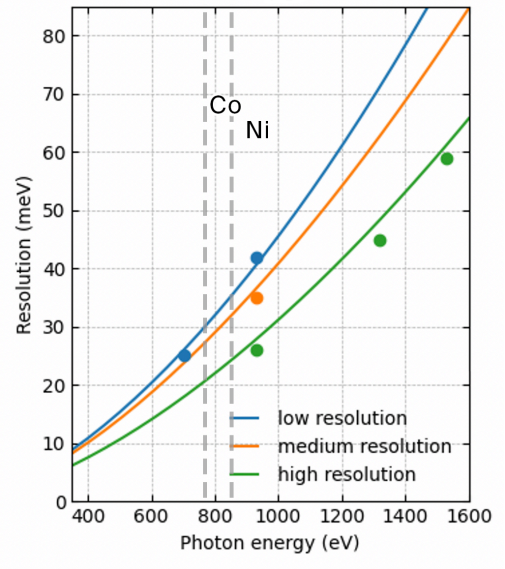

Figure 3.9: The resolution of the ID32 RIXS spectrometer as a function of energy. The gray vertical lines are in correspondence with the cobalt and nickel edges respectively. Adapted from [41].

The energy resolution of the instrument is not absolute and depends on the specific edge of measurement, and thus on the incoming photon energy. Its final value depends on the vertical spot size, the line density of the grating and the pixel size at the detector. For our measures we had FWHM $\approx$ 30 meV (see fig. 3.9).

The focused beam, impinging the probed material, has a spot size which usally depends on the many parameters of the setup as well. It usually reaches around FWHM $\approx$ 2.5 μm in height and FWHM $\approx$ 50 μm in width.

XAS can be also performed in the RIXS spectrometer in Total Electron Yield (TEY) mode by simply measuring the sample drain current (see section 4.1.3). This allows us to choose the energy for the RIXS spectra, which are in correspondence of absorption peaks. Moreover, it is used to locate the best sample areas, to check the degree of possible contamination and to evaluate the level of degradation of surface due to the X-ray beam exposure. Moreover, in our case, XMCD measures were performed as an alternative to those in the dedicated branch (section 4.1.3). This is simply done by taking two spectra around the edge of interest with opposed circular polarizations, and by taking a difference afterwards. This gives magnetic information on the sample, and was used qualitatively to determine the preferential direction of magnetization.

3.3 RIXS and magnetic excitations

It was not obvious from the beginning that RIXS could be used to probe magnetic excitations. In fact, it is generally true that photons can't couple with electron spin as a unitary change in magnetic moment $\Delta S = 1$ is usually forbidden in first order dipole transitions. Being a second order process, RIXS does not strictly adhere to this assumption, and the presence of an intermediate state completely changes the problem. One paper addressing this is the one published by van Groot et al. [46] in 1998. Here the possibility of localized spin flips in RIXS is taken into consideration as a relaxation channel mediated by strong orbital momentum coupling. The paper focuses on 3p electrons for copper and 2p electrons for nickel, but the method is general. Selection rules and polarization dependence is also obtained in the paper. The extension to proper spin waves can then be done by considering that also the incident beam acts on the many electrons of the system at the same time [14]. In a 2008 paper by van den Brink [47] a comprehensive theoretical model for spin wave RIXS is proposed. Starting from the same Heisenberg Hamiltonian of eq. (2.3), the scattering amplitude $\mathcal{F}_{fg}$ is computed as a series expansion of the hamiltonian H_0. It is found that, using a ultra-short lifetime approximation, a momentum dependent four-spin correlation function is what is measured in experiments, by including the modification of exchange correlation due to the presence of an intermediate electron hole.

$$\mathcal{F}_{fg} = \frac{U_C^2}{U^2 - U_C^2} \cdot \frac{\langle f | \sum_{\mathbf{k}} J_{\mathbf{k}} S_{\mathbf{k}-\mathbf{q}} S_{-\mathbf{k}} | g \rangle}{(\hbar\omega_{\mathbf{k}} - i\Gamma)(\hbar\omega_{\mathbf{k}} - i\Gamma - \hbar\omega_{\mathbf{k}'})} \tag{3.7}$$

Here U is the onsite electron repulsion, just like in section 2.2, while U_C is its modified value due to the core hole, and the expression in the braket is the fourier-transformed Heisenberg hamiltonian.

As soon as the resolution of RIXS spectrometers went under the 1eV regime with AXES and SAXES [44, 45] (see the next section), the possibility of using the technique as a probe of magnetic excitations became of experimentally possible as well, as spin waves started to be observed in typical ferromagnetic and antiferromagnetic materials. A good example is for instance the paper by Braicovich et al. [17] where the antiferromagnetic spin wave dispersion of La_2CuO_4 agrees with both theoretical predictions and previous neutron data (See fig. 3.10, note that the dispersion does not have the typical quadratic shape as discussed in section 2.2 due to the difference between ferrromagnetic and antiferromagnetic systems). After benchmarking paradigmatic 2D and 3D Heisenberg materials like this, in order to test how comparable the data was with existing knowledge, research turned to novel materials and started to have increasing importance in the field of high T_C superconductivity as a strong explorative tool [14, 40].

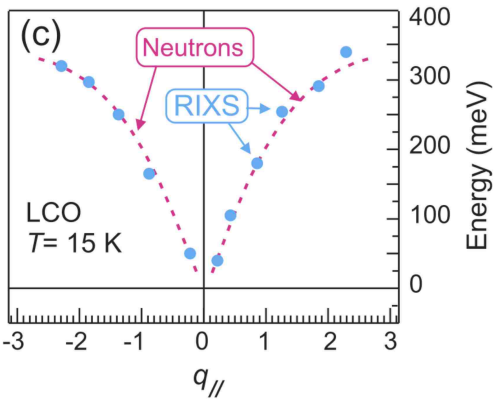

Figure 3.10: The spin wave dispersion for the antiferromagnetic compound La_2CuO_4. The purple line if fromneutron measurements, while blue dots are from RIXS. Taken from [17].

The use of the Heisenberg model in the theoretical approaches presented above could be criticized with similar arguments to those in section 2.2, as in our case we are dealing with nonlocalized materials. More in general, all of what has been put in this section is part of a quite extensive literature that deals with cuprates and other strongly correlated materials. The assumption that the theoretical justifications can be translated to metallic ferromagnetic materials seems innocuous, but together with the open questions on the nature of metallic spin waves, puts an interesting starting point for experimental investigation. We will discuss the state of the art in section 3.4.

3.4 RIXS studies on Spin Waves in metals

As anticipated in section 3.3, RIXS spectroscopy has very rarely been applied to the study of metals. This is possibly due to the intrinsic need of preserving good vacuum after the sample is prepared, as opposed to oxides, or because one has to deal with the much higher fluorescence yield. The experiments presented in this work are a direct follow-up of a previous series of measurements done by the same group at ID32, led by Nicholas Brookes. Most of the information on these is contained in ref. [22], and we summerise it shortly in this section.

RIXS measurements were performed on two fcc crystals along the [111] direction at the ID32 beamline of ESRF. As the setup is very similar to the one of the final experiments, details are discussed in section 5.1.

The first sample is an epitaxically grown iron fcc film of around 10 nm. Here a spin wave dispersion is clearly found, and it's in great agreement with previous neutron measurements (see fig. 3.12a) and in reasonable similarity with theoretical calculations, which underestimate the stiffnes D. The novelty of RIXS that can be immediately appreciated is that the same dispersion of INS is obtained by a much smaller sample, of around 10 nm.

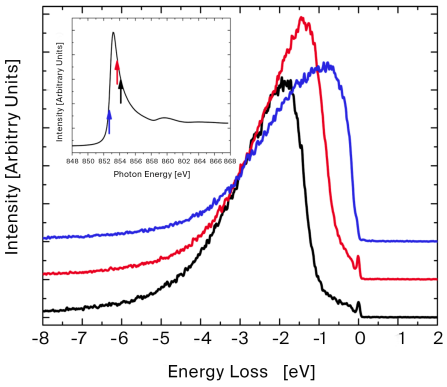

Figure 3.11: The effect of detuning the incoming energy on the RIXS spectrum. The arrows on the inset show the value of energy of each. Taken from [22].

The second sample is a nickel single crystal, cleaned with repeated cycles of Ar^+ sputtering with subsequent annealing. In the spectra, the fluorescence has a much closer position to the zero with respect to the iron sample, and its tail covers the sought magnons. Incoming energy is then detuned, slighly moving up of 1 eV from the nickel L_3 edge (see fig. 3.11). At difference with iron, the spectra does not adhere with neutron data in the high momenta range (see fig. 4.10). As opposed to iron, here calculations seem to overestimate D. In the paper, possible options are considered: this energy discrepancy at high q could be ascribed to the interaction with the Stoner continuum, that ends up in a damping [2], but this is not supported by the calculations [22].

A more accurate study of fcc nickel is required, and it is thus the starting point of this work.

In what follows, the difference between the two dispersions is also explored through the measure of an electronically in-between case: fcc cobalt. Here correlation effects, that are stronger than in iron, should still play a smaller role than in nickel. The idea is that if the behaviour seen in nickel is of physical nature, it should appear to some extent in this sample as well. Note that this is valid also for the comparison with ab initio calculations: between the two computed values of D, one overestimating and the other one underestimating, we should have an intermediate situation.

Although not the thermodynamically stable configuration of the metal, which is usually hcp, fcc cobalt is fairly easy to obtain epitaxially. For this reason this system has not been studied by INS: the intrinsic need of bulk samples makes any study of thermodynamically unstable materials impossible, as they can't grow up to macroscopic single crystals. The solution usually employed is to use alloys which stabilize the system of interest: fcc cobalt for example is thermodynamically favoured with the presence of 8% iron in its structure, as studied by Sinclair et al. [11].

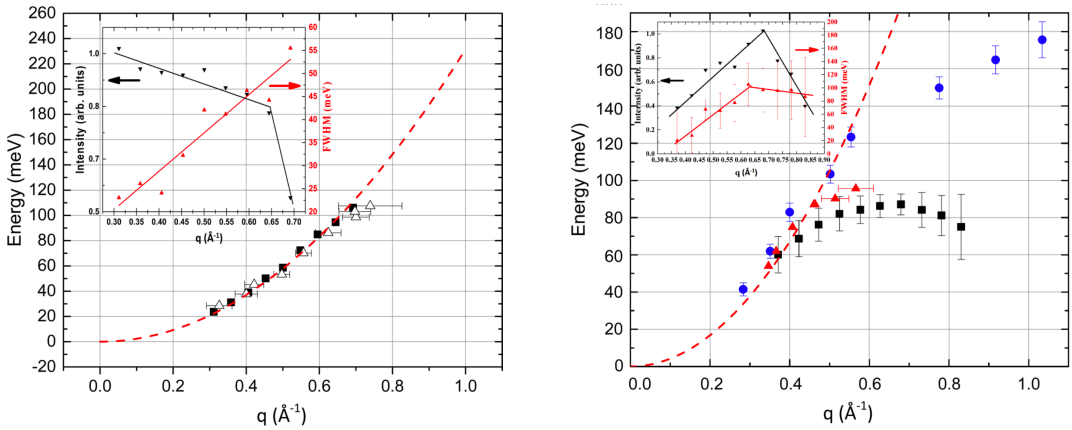

(a) Iron spin wave dispersion.

(b) Nickel spin wave dispersion.

Figure 3.12: In (a), black squares are RIXS data while white triangles are from neutron measurements. In (b), black squares are RIXS data while blue dots and red triangles are from neutron measurements. Taken from [22].

It shall be noted that another work on metallic RIXS was performed recently in Brookhaven by Pelliciari et al. [23]. Here the spin wave dispersion of iron and its thickness dependence, from bulk down to a film of three unit cells, are measured. The same idea of reducing the sample thickness with respect to INS is then exploited. The dispersion is shown to change as the stiffness gets lower for thinner films. This work shows an interesting use of RIXS that could be explored in the future and, together with the measurements performed here at ID32, clearly demonstrate the possibility for Resonant Inelastic X-ray Scattering to see and accurately probe spin waves and their dispersion.

Chapter 4

Sample Growth and Characterization

In this chapter we address the techniques that have been used to both obtain and characterize the samples of interest.

The aim of our research was to measure spin waves in two ferromagnetic metals, cobalt and nickel. As the study of spin waves and their dispersion is of course q-dependent it was mandatory to have a single crystal sample. This, together with the presence of the sample preparation facility in close contact with the spectrometer of the ID32 beamline, led the choice of growing the metallic films epitaxially.

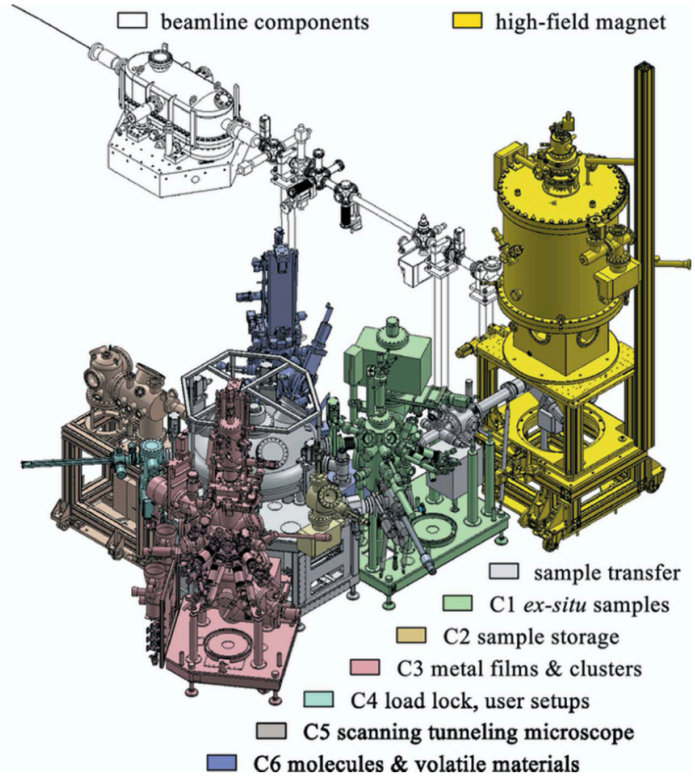

Figure 4.1: The whole sample preparation facility and high-field XMCD endstation. Taken from [48].

It is known that the two metals of interest tend to grow with an fcc structure when evaporated on a copper [001] surface (see for example refs. [49, 50, 51] for nickel, refs. [52, 53] for cobalt). The choice of film growth takes advantage of one of the differences between RIXS and INS: while the latter needs macroscopic bulk materials to significantly scatter neutrons, the former only needs a few hundred micrometers in area and a few nanometers in depth. Epitaxially growing one's own samples gives some additional advantages: the film is "fresh", it can be prepared just before experiment with as little exposure as possible, and the recipe can be tested and refined in advance to ensure a correct crystalline purity and absence of contamination.

Molecular beam epitaxy also gives much more freedom in the choices of growth. As the process does not take place at thermodynamic equilibrium, cobalt can grow easily outside of its normal hcp phase, growing as fcc instead. This couldn't happen in macroscopic samples, where the solution is usually to employ alloys [11]. Finally, for reasons that will be made clear in section 4.3, it also let us deposit a cobalt buffer layer in a nickel sample to force its magnetization in the planar direction.

One has to consider that photon scattering does need some amount of material to have reasonable counting times for the spectrometer. Moreover, our interest was to compare data with INS experiments, either directly or for similar systems, where the spin wave dispersion is that of a bulk sample. For these two reasons, growth was performed to obtain samples in the orders of 1 to 10 nm.

Characterization was done on both test samples and in the final ones as well to ensure crystal degree of order, to check for any kind of contamination and to investigate magnetization. The methods used are all well established. In particular, magnetic characterization was also performed using the XMCD endstation at ID32 [48].

The ID32 beamline at ESRF combines a flexible design that lets samples be moved through different chambers effortlessly [48]. All growths took place in the so called "metal chamber" (C3, pink in fig. 4.1), which contains all the needed instruments to perform epitaxy and basic characterization. UHV is ensured in all the environments: specifically, the pressure of our chamber was in the low 10^{-10} mbar regime.

4.1 Characterization Techniques

The methods used to characterize our samples are reviewed in the following section with their theoretical basis and technical implementation, and are treated with particular attention towards the information highlighted by each, trying to relate each output to how it's useful and how it has been employed in our case. The information presented is not meant to be exhaustive, as many other sources of information already exist in the literature.

4.1.1 Low Energy Electron Diffraction

To investigate the crystaline structure of our samples and their surface, Low Energy Electron Diffraction (LEED) was used. The aim of this technique was in our case to have a qualitative picture of the atomic ordering in the sample: the output of a LEED measure is a diffraction pattern, generated on a phosphorescent screen and possibly captured by a camera, that is then compared with theoretical knowledge about the lattice structure and with previous data. The width of the diffraction peaks gives information on the degree of ordering of the crystal structure, while the presence of extra peaks is a sign of contamination or reconstruction.

LEED [54] is nowadays mature and commonly employed in a vast range of laboratories as a feasible alternative to X-Ray Diffraction, with the biggest differences being its sensitivity to surface instead of bulk. The need of a UHV environment, which made LEED difficult in its

first appearances, is nowadays obtained with little difficulty and, in our case, granted as of mandatory importance for the growth itself [48].

The energy range in which collimated electrons have comparable wavelength to interatomic spacing (circa 1 Å) is around 20-500 eV, which is when their inelastic mean free path is the smallest, usually a few monolayers [55]. This justifies the fact that LEED is a surface technique, in opposition to X-Ray Diffraction where penetration depth is in the order of microns. It should be noted that the energy dependence of the inelastic mean free path tends to follow a "universal curve", more or less valid for the majority of diffusive media of interest, and thus this assumption is valid in general [56].

Recalling the Von Laue Condition, one has diffraction peaks when a generic beam satisfies:

$$\mathbf{G} = \mathbf{k}' - \mathbf{k} \tag{4.1}$$

where $\mathbf{k}$ and $\mathbf{k}'$ are wavevectors of the incoming and outgoing beam, while $\mathbf{G}$ is a vector identifying a point in the reciprocal lattice of the probed crystal. As we consider elastic scattering, one has $|\mathbf{k}| = |\mathbf{k}'|$: this lets us look at eq. (4.1) geometrically, as the condition is satisfied when the points of the reciprocal lattice belong to a sphere of radius $|\mathbf{k}'|$, sharing the same center. This picture is due to Ewald and the constructioin is often referred to as Ewald Sphere [57].

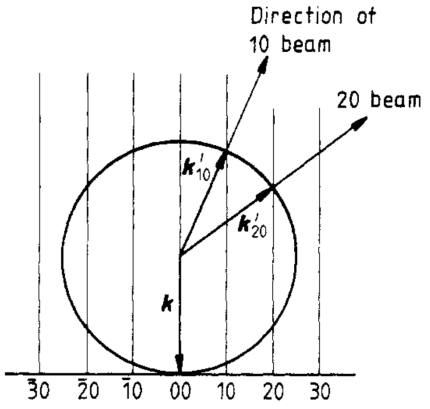

Figure 4.2: The Ewald sphere intersecting the recitprocal lattice "rods". Taken from [55].

We have seen that LEED only probes the surface of the sample: we then intuitively take this as if the crystal, instead of a plane, was three-dimensional with an infinite spacing between each of the planes. As lengths appear at the denominator of reciprocal base vectors, we'll end up with infinitely close dots ("rods" or "lines") instead of points in our reciprocal lattice, as in fig. 4.2. Adjusting the energy of the beam results in a change in the radius of the Ewald Sphere: the presence of "rods" lets us always end up with the diffraction condition satisfied as long as we exceed the energy of the first order peaks. In our case, where we worked with a length of a $\approx$ 3.5Å, the first order peaks appeared at around V = 67eV.

A typical diffractometer for LEED crystallography usually follows a simple scheme as in fig. 4.3 . The grounded sample is hit by a beam of focused electrons coming from an electron gun where they are extracted by thermoionic effect. Once the surface has been hit by electrons, only a small percentage diffracts elastically. To get rid of lower

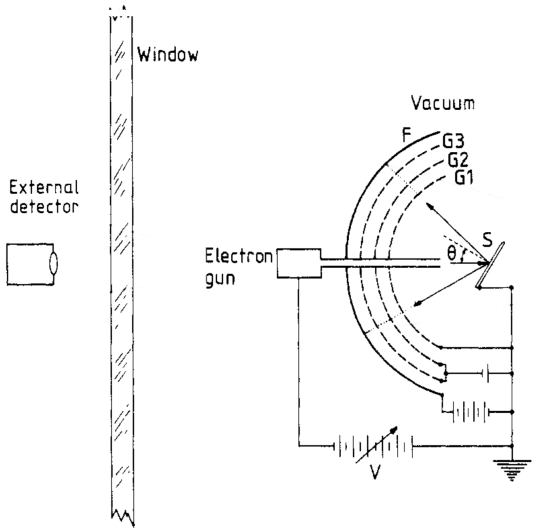

Figure 4.3: Rear view LEED configuration. Adapted from [55].

energy electrons, scattered inelastically in all directions, a negative potential is applied between two grids (G1 and G2 in figure). A stronger positive potential is then applied between a further grid and the phosphorescent screen (G3 and F), to reach the latter with high enough energy to impinge it and make it glow. The same screen is visible from outside the UHV chamber. The instrument present at the Sample Preparation Facity of ID32 is a commercial rearview LEED provided by VacGen.

The type of monitoring done was of two kinds. Spot size was a qualitative indicator of long range crystaline order. It might happen that diffraction peaks appear in the correct position, but with a too broad shape: this is intuitively explained by a less ordered sample. Alternatively, if new peaks appear within the known ones, adsorption has taken place: when this happens in a periodic manner, spacings are usually bigger than the ones of the substrate, and thus appear as closer points in the diffraction pattern. Moreover, disorder and contamination can also be seen in the form of a relative higher background.

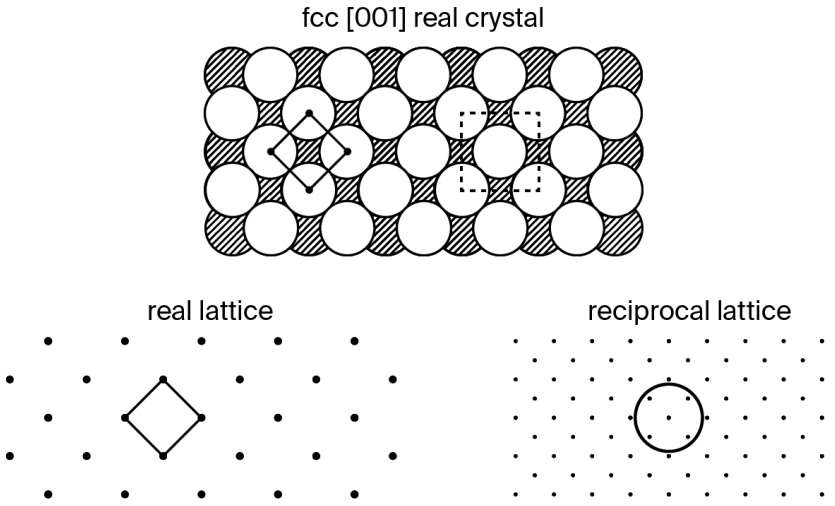

Figure 4.4: Schematic depiction of a fcc [001] surface, with its face highlighted by the dashed square. The measured LEED pattern is the one on bottom right. The circle represents a possible field of view of the instrument.

We can now restrict ourselves to the specific case of our samples: all substrates and films were fcc crystals cut on the [001] face, with the [100] direction aligned to the horizontal axis. As shown in figure fig. 4.4, the resulting surface geometry is the one of a simple square lattice with size $a = a_0/\sqrt{2}$ tilted of 45°. As the reciprocal of a square lattice is again a square lattice, the resulting LEED pattern is as in fig. 4.4.

LEED was performed to calibrate the cleaning process in order to make it effective and quick. It was also done after each growth, be it a test one or a definitive one, to check the overall quality of the sample.

4.1.2 Auger Electron Spectroscopy

Auger Electron Spectroscopy (AES) is a analytical technique of popular use in the field of surface characterization. It is often considered as semi-quantitative; indeed even in our case most of the information was drawn from qualitative analysis of recorded spectra, while some calculation was performed only to confirm assumptions based on complementary data.

The Auger Process, discovered independently by Lise Meitner and Pierre Auger in the 20s [58], is one of the possible relaxation channels through which a core hole, usually generated by an energetic electron beam, (that we take at E_0) in an atom is filled by a more energetic electron (initially at E_1). Instead of emitting a photon, the excess energy is absorbed by a second electron (initially at E_2) that is then expelled freely with a residual kinetic energy:

$$E_k = (E_1 - E_0) - (E_F - E_2) + (-\phi) \tag{4.2}$$

where ϕ is the work function of the specific material and E_F is the Fermi Energy. E_F can be arbitrarily set as the 0 of the energy scale, while ϕ is calibrated.

It is important to see that the Energy of emitted Auger electrons E_K is independent from the way in which the first core-hole is generated, which is usually an electron beam of given energy. Note that E_1 and E_2 (see fig. 4.5) can be any of the many occupied states, even coinciding: there are many Auger lines depending on which electrons fill the holes and which are ejected. Each transition is recognized an labelled depending on these three involved levels, E_0, E_1, E_2.

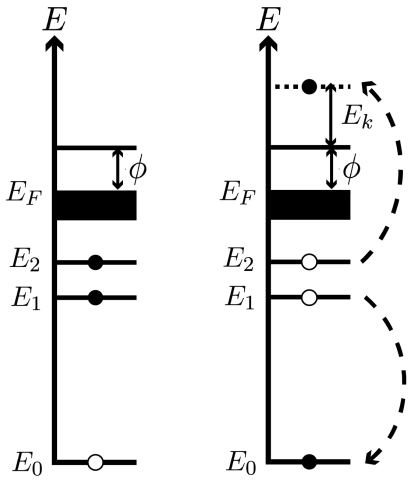

Figure 4.5: Energy level diagram for the Auger process.

The valence band just below E_F is responsible of a cascading effect that contributes to the high number of low energetic electrons in the first region of the spectrum, as the vacancies left in the first process generate other Auger decays and so on, with increasingly lower kinetic energies. This phenomena, known as electorn yield, is at the basis of XAS measurements described in the next section.

Following a similar reasoning to the one of LEED, it can be easily seen that AES is a surface technique as well, as the inelastic mean free path of Auger electrons is still the bottleneck of the detection process. In this case, the depth of measurements is of around 100 Å as the kinetic energies of emitted electrons, for instance in the case of copper, lie in the 60 to 1000 eV range.

Typical Auger spectra display a high background and broad peaks. The reason for the former problem resides in the presence of backscattered electrons together with Auger ones, while the latter is related to the short lifetime of the core-hole state [59, 60].

AES counts the number of Auger electrons emitted at each E_k, resulting in an energy spectrum for a range of choice. As in many other spectroscopy techniques, the peaks are specific of each element on the surface of the material (an thus act as "chemical footprints" for it) and can be either computed numerically or, if the technique is mature enough, compared with known literature. As this is the case of AES, our main choice of reference was the Handbook of Auger Electron Spectroscopy [61].

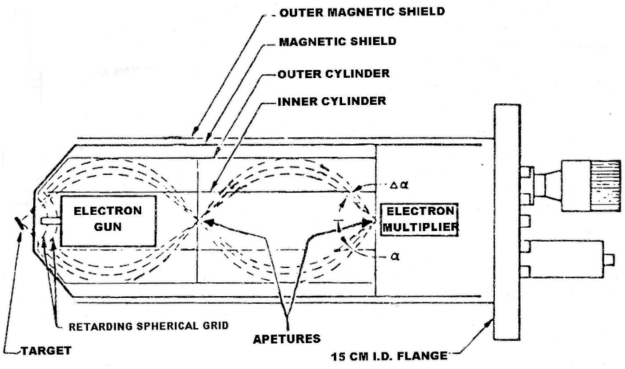

Figure 4.6: The double CMA implementation of an Auger spectrometer. Taken from [62].

The technical implementation of AES is nowadays pretty standard, but subtle differences exist. I describe it in what follows focusing on the specific setup of the instrument present at the ID32 Beamline. The spectrometer is a STAIB DESA 100 double-pass CMA, and can be used in both lock-in and pulse counting modes [48]. To ionize the atoms of the sample at their core level, a collimated electron beam of usually 3 KeV is used, providing a current in the order of 10 μA. The Auger electrons generated by the incident electron beam with the sample must then be analyzed: there must be detector able to proportionally count the number N of electrons produced at each E_k. This is done by a Cylindrical Mirror Analyzer (fig. 4.6): a potential that lets electrons with only a specific energy reach the end of the device, acting as a very narrow band pass filter. The signal is then amplified by a channeltron.

Our measurements were restricted to pulse counting mode, which have a small difference in comparing spectra with literature, which are usually displayed as derivative.

Spectra were usually taken in the 500 to 1000 eV range, where both the main features for all three elements used (cobalt, nickel, and the copper substrate) and the eventual presence of oxygen, sign of contamination, were visible. In fig. 4.7 the three characteristic spectra of the elements we used, cobalt, nickel and copper, are shown.

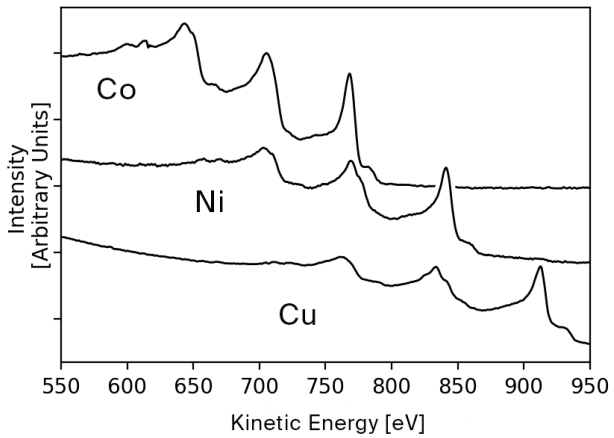

Figure 4.7: Auger spectra measured during the preparation of our growths.

4.1.3 X-Ray Magnetic Circular Dichroism

The branch of the ID32 beamline where the sample preparation and characterization takes place, that I describe throughout this chapter, has its centerpiece in the X-Ray Absorption Spectroscopy endstation for X-Ray Magnetic Circular Dichroism and X-Ray Magnetic Linear Dichroism (XMCD and XMLD respectively).

X-Ray Absorption Spectroscopy (XAS) is nowadays a much used technique for sample char-

acterization and analysis. When the beam impinges the material, electrons from low energetic states are excited to higher energy ones by photon absorption, resulting in a decrease in intensity. If the change in intensity is evaluated over a scan of some hundreds of electronvolts, the final spectra reflects the local properties of the electronic structure of the probed material, in particular of its empty states, showing peaks corresponding to the transition of each element as well as new information on their environment [63]. This excitation process is the same at the base of RIXS. XAS is in fact used to determine which are the resonances (edges) for inelastic scattering (fig. 4.8).

The need of tunable X-rays, that are swept in each measurement over such a long photon energy range dictates the need of synchrotron light. The measure can be performed in either Total Electron Yield (TEY), based on the cascading of low energetic Auger electrons, or Total Fluorescence Yield (TFY). Both of the two always take place, but with different probabilities. As for small atomic numbers almost 99% of the decay usually happens by means of Auger yield, our XAS measures are usually restricted to TEY.

XMCD and XMLD are based on the idea of considering the polarization of the incoming beam as the new degree of freedom of the experiment. For the former case, differences in XAS spectra acquired with different circular polarizations (clockwise or anti-clockwise) reflect the presence of magnetization in the sample, as some excitation channels for spins with parallel (or antiparallel) direction to the beam are favoured. Note that this only happens if the sample is ferromagnetic or ferrimagnetic, with the presence of a net magnetic moment component along the beam direction. If the difference between two XAS spectra is taken, usually normalized to the sum of the peaks for the two polarizations, an XMCD spectrum is obtained [64]. If one looks at the XMCD main peak, its value can be read as a percentage of the main peak total intensity. This value is usually referred to as "dichroism", and if μ_+ and μ_- are the peak heights for clockwise and anti-clockwise polarizations XAS, it can simply be written: as

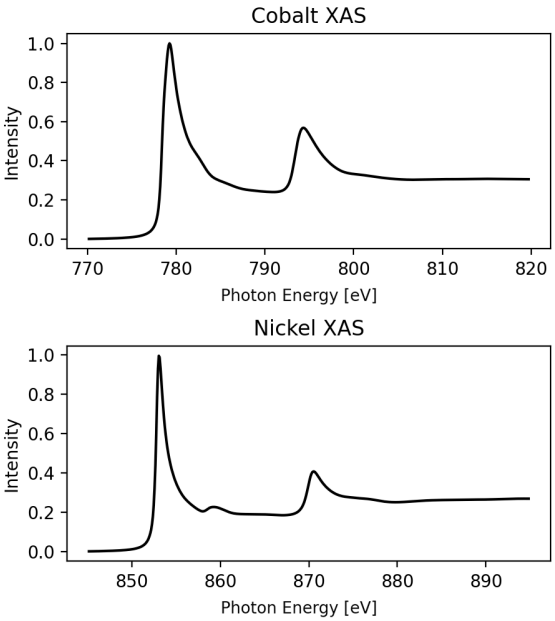

Figure 4.8: Normalized XAS for thin films of cobalt (7 nm) and nickel (5 nm) grown for our experiments.

$$D = \mu_+ - \mu_- \tag{4.3}$$

Just as with XAS, this value strictly depends on the material and on its magnetization. If it is lower than expected, there might then be presence of a multi-domain structure, or magnetization could not have taken place fully. In more refined applications, a quantitative approach can be used to evaluate the spin and orbital magnetic moment of the atoms, by what are known as "sum-rules" [65, 66, 67].

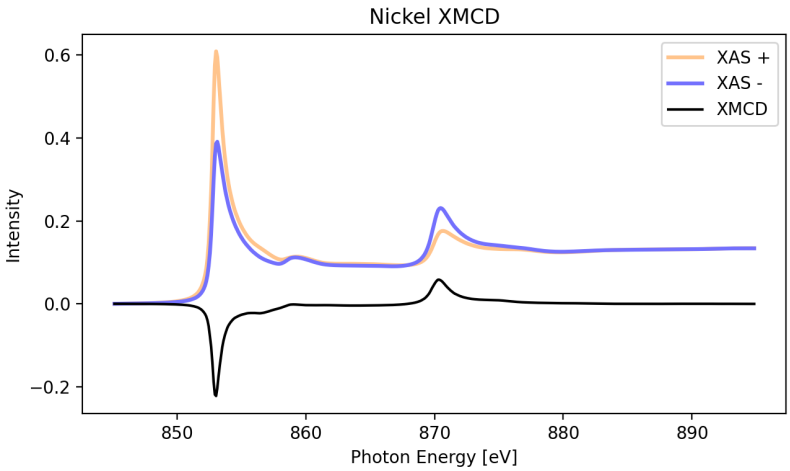

Figure 4.9: XMCD for a strongly magnetic nickel sample.

The instrument at ID32 (yellow in fig. 4.1) was designed for fast and reliable user measures, with the ability to operate with ease even at extreme conditions: the temperature of the sample can reach down to 5K while two superconducting magnets of 9T and 4T (perpendicular and parallel to the beam) allow magnetic field dependent measurements. The sample is mounted on a manipulator that allows rotations in the horizontal plane as well as translations, allowing normal and grazing incidence measurements. Both TEY and TFY are performed by measuring the drain current of the sample and with an IRD photodiode respectively [48].

In our case the set of measures was quite simple: all ferromagnetic metals have high enough Curie Temperature to work safely at ambient temperature [3]; moreover, the order of magnitude of their coercive field is well below 0.1 T. Our aim was understanding the presence and direction of magnetization, by looking at both grazing and normal XMCD. As we are dealing with films, shape anisotropy lets either planar or normal magnetization prevail over the other. As we will see in section 5.1, this work highlights the importance of knowing the direction of magnetization, as it influences the geometric RIXS cross section.

After the characterization of some test samples, later XMCD spectra were taken in the RIXS spectrometer just before measurements. Here, the only difference was the inability to magnetize the sample at will: they had to be measured in remenance.

4.2 Epitaxial Growth of metals

Generalities on the preparation of samples are discussed in this section, from the treatment of the substrate to the growth of metals.

4.2.1 Substrate Preparation

For the growth, high purity fcc copper monocrystals cut on the [001] face have been used as substrates. All of them had been manually aligned to have the [100] direction parallel to the horizontal axis with an estimated error of $\pm$ 3°.

The substrate was cleaned before each growth with repeated cycles of Ar^+ sputtering (P = $8x10^{-6}$ mbar with an applied voltage HV = 1 kV) of 30 minutes and subsequent annealing at T=600°C for 20 minutes [51, 50, 49]. If metal from a previous evaporation was needed to be removed, a higher energy of HV = 1.7 kV was used for 1 hour during sputtering.

AES was performed prior to annealing to ensure the absence of any adsorbant, be it from the chamber atmosphere (Carbon and Oxygen) or metal left from previous growths. In fact, heating the sample even at low temperatures favors interdiffusion, the substrate forming an alloy with the absorbed metal in an irreversible manner. LEED was used to determine the crystalline quality of the substrate surface before proceeding with epitaxial growth. The cycling usually stopped when the main diffraction peaks were sufficiently sharp, as in fig. 4.10a. After some trials, a good recipe was found that was able to obtain sufficiently clean surfaces after only one cycle.

When the surface was considered clean and ready for evaporation, it stayed exposed to an atmosphere of low 10^{-10} mbar for no more than a few hours.

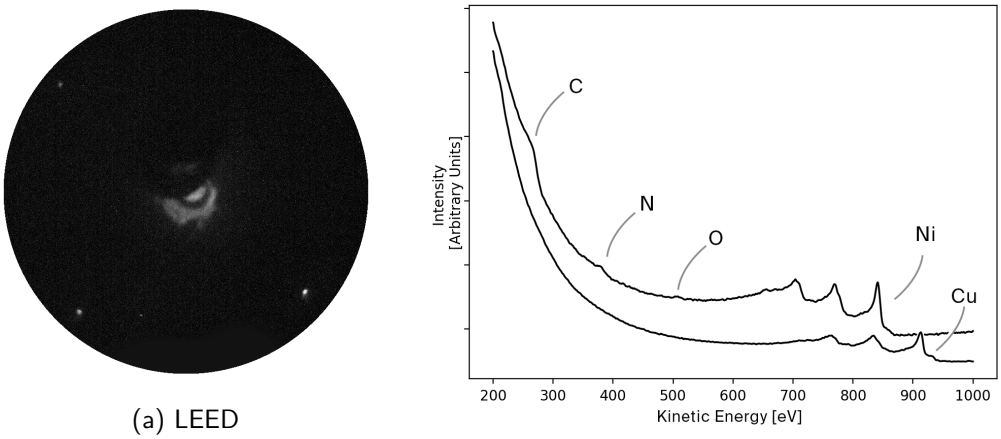

(a) LEED

(b) AES

Figure 4.10: (a) is a LEED diffraction figure of a clean Cu[001] surface. The top right peak is not visible due to a vertical tilt in the manipulator position. V = 67 eV. (b) shows the cleaning process, from a dirty thin nickel film (top) to its substrate (bottom), where only copper is present.

4.2.2 Molecular Beam Epitaxy

From its first appearances in the 70s Molecular Beam Epitaxy has developed into being one of the most established technologies for film growth in general. At variance with other approaches, it is one that combines ease and reproducibility with a high degree of accuracy: films can be grown with sub-monolayer precision, and at the same time, being an intrinsically physical process, the growing conditions are not the ones of thermal equilibrium expanding the range of possible atomic structures [68].

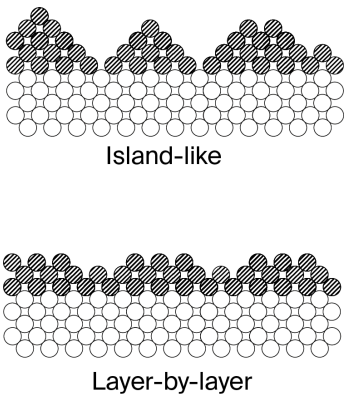

Figure 4.11: The two modes of growth of MBE.

The word epitaxy comes from "arranging upon", to indicate the act of building a sample by depositing atoms on a substrate. There are however many ways in which this process takes place, and not always complete control is granted. Depending on the mobility of the adsorbed evaporant, the growth can be "island-like", whenever a new layer starts to grow before the previous finishes, or "layer-by-layer", in the opposite case (see fig. 4.11). For metals, a low mobility usually ensures the latter, which is preferable for our case where we ideally want a flat surface (see for example refs. [51, 50, 69]).

In ref. [70] nickel MBE is studied with Scanning Tunnel Microscopy and is shown to display island behaviour to a little degree, as clusters appear before the complete covering of one layer. The paper suggests a soft annealing at T=100°C for a few minutes to increase interdiffusion and fix the problem, but this step was considered unnecessary for the scope of the work.

EBM is performed with Evaporators. These pieces of equipment carry out the simple task of bringing the evaporant, the material of interest mounted by the user in its solid phase, to sublimation. Heating is performed in our case with an electron beam of controllable power. Sublimation can be seen as the change in vapor pressure when the solid material is brought to high temperatures (of the order of thousands of degrees Celsius), and that then results in an extended column of gas spatially going from the evaporant to the substrate. The rate of evaporation is roughly measured by a fluxmeter, which measures a drain current from the top of the evaporator, proportional the number of the gaseous ions. It is this reading that ensures stability and reproducibility of evaporation rate. As the evaporant reaches temperatures in the range of thousands of degrees Celsius, water cooling is needed to protect the instrument.

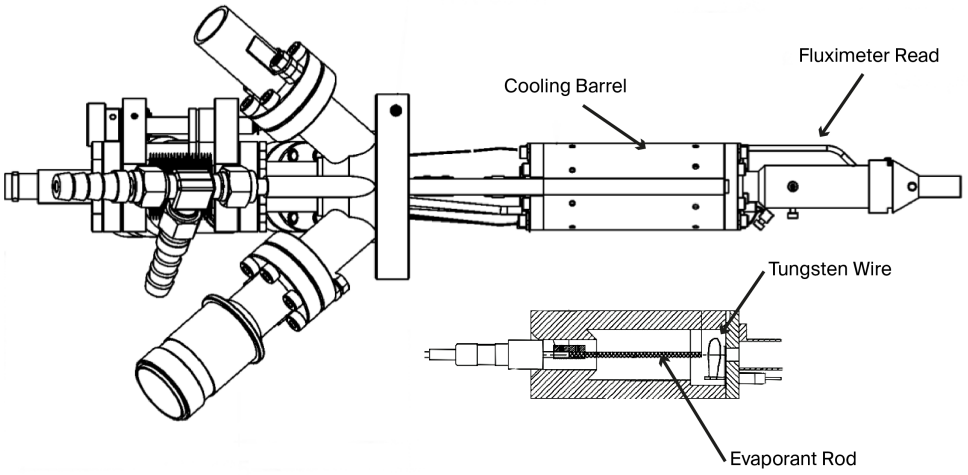

Figure 4.12: Drawing and section of the Omicron Evaporator used. Adapted from the Instrument Manual.

To monitor a more effective measure of evaporation rate a quartz crystal microbalance is employed [71]. A quartz piezoelectric disc is used as resonator and put in oscillation: changes in its frequency are linked to the differential absorbed mass of evaporant metal, providing good estimates under some simplifying assumptions.

For our samples, 3 UHV EFM3 Focus Omicron Evaporators (fig. 4.12) were used, with nickel and cobalt mounted as rods. The electron beam is provided by thermoionic electrons emitted from a tungsten wire, accelerated by a high voltage.

4.3 Cobalt and nickel growths

Now that all the tools used in the preparation and characterization phase have been presented, we can look at the final samples of interest.

The Evaporators were calibrated using the quartz crystal microbalance: different configurations of current, voltage and rod positioning were tried until a good evaporation rate was established.

Once done, the conditions are reproduced and kept constant by looking at the fluxmeter. Due to the thickness of the final sample, a repositioning of the rod was required from time to time.

For cobalt, evaporation reached a rate of circa 1.2 Å/min , while for nickel it was slightly less, of around 0.85 Å/min.

Each growth started from a clean Cu[001] sample, displaying a sharp LEED pattern and no contamination in AES, as soon as temperature reached T = 30°C (see fig. 4.10a). During the growths, pressure usually stayed in the mid 10^{-10}mbar regime.

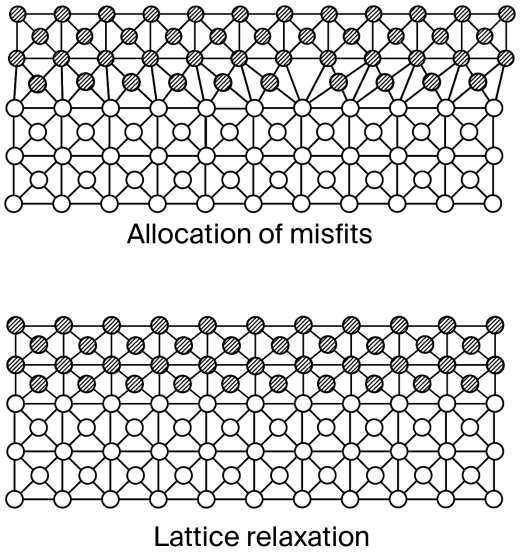

Figure 4.13: The two types of growth expected for nickel (top) and cobalt (bottom).

We shortly cover an issue that is very general whenever the growth is heteroepitaxial, meaning one has two different materials one on top of each other. It must be taken into account that there will be a mismatch in lattice constant between the two. The growth is called pseudomorphic when, as in our case, this difference is of few percents: copper has a lattice parameter of $a_0 = 3.61$ Å [72], which is larger than the two evaporated materials.

Nickel has a lattice parameter of $a_0 = 3.52$ Å [72]. Its growth on copper has been studied in depth, and it was shown to follow the Frank-van der Mewe model [73]: the lattice stretches to match the underlying copper layer as long as a critical length is reached; after that, the lattice relaxes to its usual dimension and misfits are introduced in the crystal. The 1970 paper by Matthews et al. [74] found this length to be of around t = 14.6 Å. As we will soon see, our growths exceeded this value, and thus we'll consider the sample as in its bulk shape (fig. 4.13, top).

As we already mentioned, the fcc structure is not a stable configuration for cobalt at ambient temperature. The value of $a_0 = 3.55$ Å was found for the range temperatures in which this configuration is thermodynamically favoured by Owen et al. [75]. However, a paper by Cerda et al. [52] suggests that, for what concerns cobalt on copper [001] surfaces, the relaxation procedure that happens in nickel (as in the Frank-van der Mewe model) does not take place. Instead, the crystal adapts its shape in a deformed fcc where the planar stretch required to match the copper lattice constant is balanced by a vertical compression. Although this was proved for a small number of monolayers, we'll use this approximation nonetheless, taking a lattice constant of the same size of copper (fig. 4.13, bottom). It should be noticed that, for the final dispersion results, using either accounts for only small changes.

At the end, two separate fcc cobalt samples of 7 nm thickness were obtained and successfully measured. One LEED pattern is shown in fig. 4.14, where of course the final layer has much broader peaks than the clean copper surface of fig. 4.10a. XMCD for both cobalt samples shows no dichroism in the perpendicular direction, and little, although visible, dichroism in grazing angle: the cobalt sample clearly shows a small planar magnetization, with the possibility of multi domain structures. When magnetized in the XMCD chamber, the full dichroism of cobalt was observed in remanence as the in-plane domains re-align themselves (fig. 4.14).

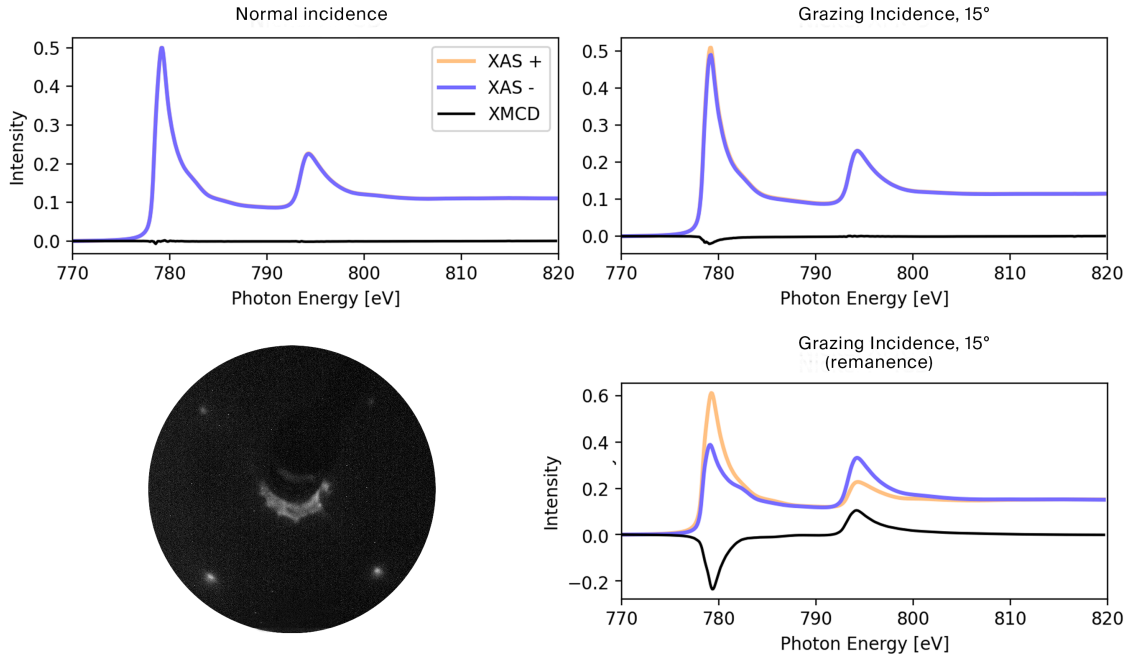

Figure 4.14: 7nm cobalt film measured in the XMCD chamber. The final samples, measured in RIXS, showed a similar behaviour to that prior to magnetizaiton. LEED of the sample is included in bottom left.

Spin wave measurements in the nickel sample proved to be harder than for cobalt, and thus more samples had to be prepared. A first sample of 5 nm was grown, and displayed strong perpendicular magnetization (fig. 4.15).

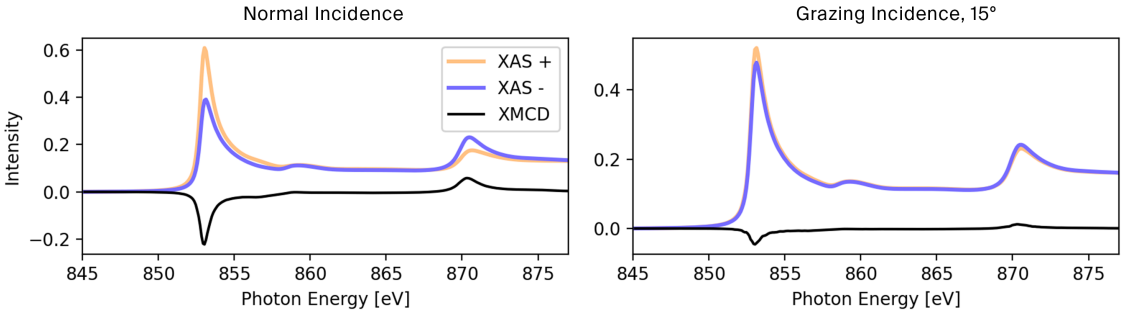

Figure 4.15: 5 nm nickel film measured in the XMCD chamber. The other 5nm sample measured in RIXS showed a similar behaviour.

It will be made clear in section 5.1 that a planar magnetization is mandatory for measuring spin waves in RIXS for the specific configuration of our experiment. A paper by O'Brien et al. [76], where thickness dependent XMCD of nickel grown fcc films is studied, highlights two magnetization transitions from planar to perpendicular at around 7 ML and from perpendicular to planar at around 37 ML (circa 9 nm). As this first sample belongs to the in-between region of perpendicular magnetization, two other samples were prepared with thicknesses of 10 and 15 nm to ensure planar magnetization. Unfortunately, XMCD of both displayed yet again perpendicular magnetization, although small. This is less visible in the 15 nm sample. This could be linked to contamination at start, as some extra spots clearly appear in the LEED

pattern of the last sample (see fig. 4.18).

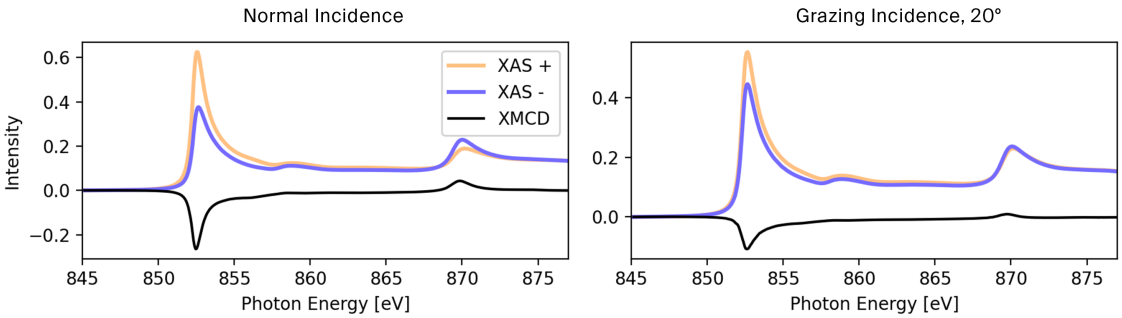

Figure 4.16: 10 nm nickel film measured in the RIXS chamber.

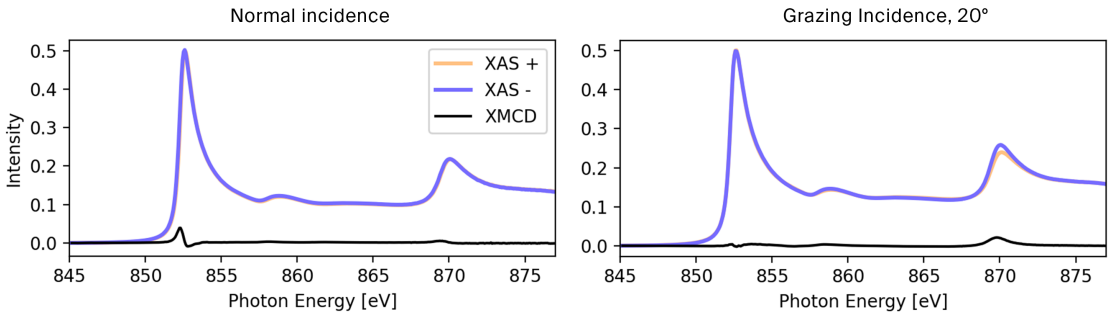

Figure 4.17: 15 nm nickel film measured in the RIXS chamber.

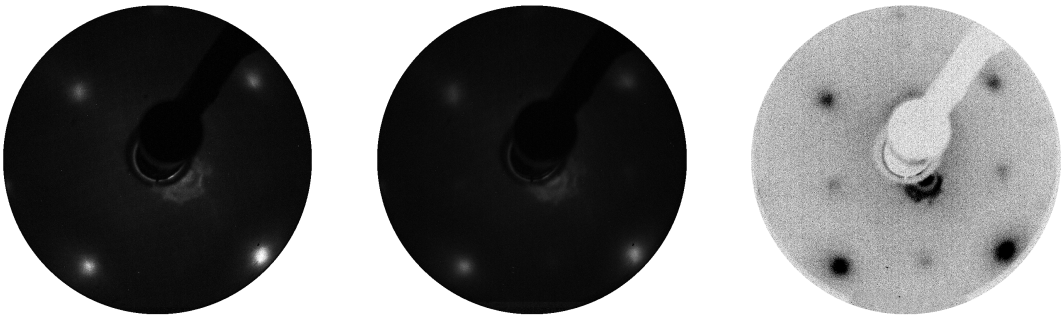

(a) Ni 10 nm (b) Ni 15 nm (c) Ni 15 nm, processed

Figure 4.18: LEED for the 10 nm and 15 nm samples. When processed, the latter shows the presence of some extra spots, which are absent in the former, signs of contamination.

An additional and final nickel sample of 7 nm was prepared over a cobalt buffer layer of 1 nm, grown on the same copper substrate. This additional layer was suggested by the same authors of ref. [76] as a solution to ensure in-plane magnetization. The growth was successful, and the XMCD spectrum showed clear, although not huge, in-plane magnetization (fig. 4.19).

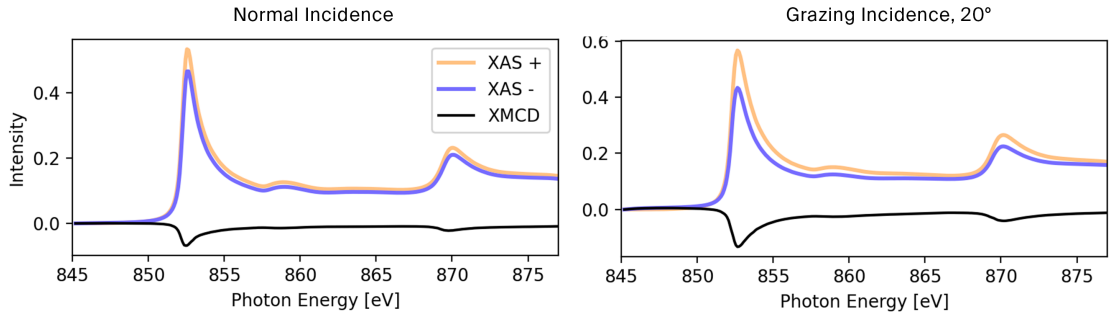

Figure 4.19: 7 nm nickel film with a 1 nm cobalt buffer layer measured in the RIXS chamber. Note that it's the first XMCD spectrum in which there is higher dichroism for the grazing angle measure.

Chapter 5

Experimental Results and Data Analysis

In this chapter we discuss the main results of our measurements. We begin by looking at the final setup of the RIXS experiment. Our main objective will be looking for the dispersion, if present, of spin waves: to properly do this, we will have to fit each RIXS spectrum as discussed in section 5.2. We finally address a comparison of our results with both experimental results and theoretical *ab initio* calculations.

5.1 Experimental Setup

After the samples were prepared as described in section 4.3, they were either directly transported to the RIXS chamber for measures or waited in a high 10^{-11} mbar vacuum for no more than a few hours.

The RIXS chamber is not directly connected to the sample preparation facility, and the samples were transported with the aid of a modified UHV suitcase provided by Ferrovac [77]. In it, a pressure of mid to low 10^{-10} mbar was provided by a getter ion pump that can run on a battery, allowing an easy and contamination-free transport from one branch to the other. The sample briefly saw higher pressures of 10^{-8} mbar and 10^{-7} mbar during the sample transfers to the RIXS measuring chamber, usually for no more than a few minutes. As the XAS of section 4.3 don't show signs of contamination, the transfer was considered successful.

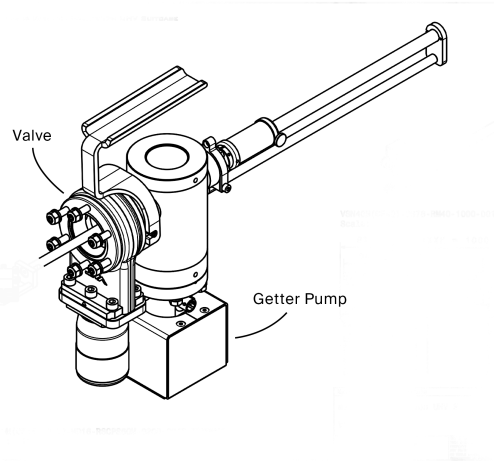

Figure 5.1: Schematics of the UHV suitcase employed for the sample transfer. Adapted from [77]

The sample was mounted on the RIXS custom shuttle. Once facing the beam, the sample needs a vertical tilt of 54.7° to reach the [0$\sqrt{}$21] position, if mounted with the [100] direction horizontal. As the goniometer only allows $\pm$ 45° rotations in the χ direction , a 20° wedge was employed. With it, the shift in χ is of only -34.7°. To go back to the [001] direction (see fig. 5.2), a tilt of $+20°$ in the opposite direction is needed. The experiments were set in a way that exploited the whole momentum range of the spectrometer.

To align the sample, the position is moved while looking at the intensity of the main XAS peak. The pressure in the RIXS chamber was of around low 10^{-9}mbar and some regions of the sample, usually those impinged with the X-ray beam, might expect some degradation with time. This possibility is again checked with XAS.

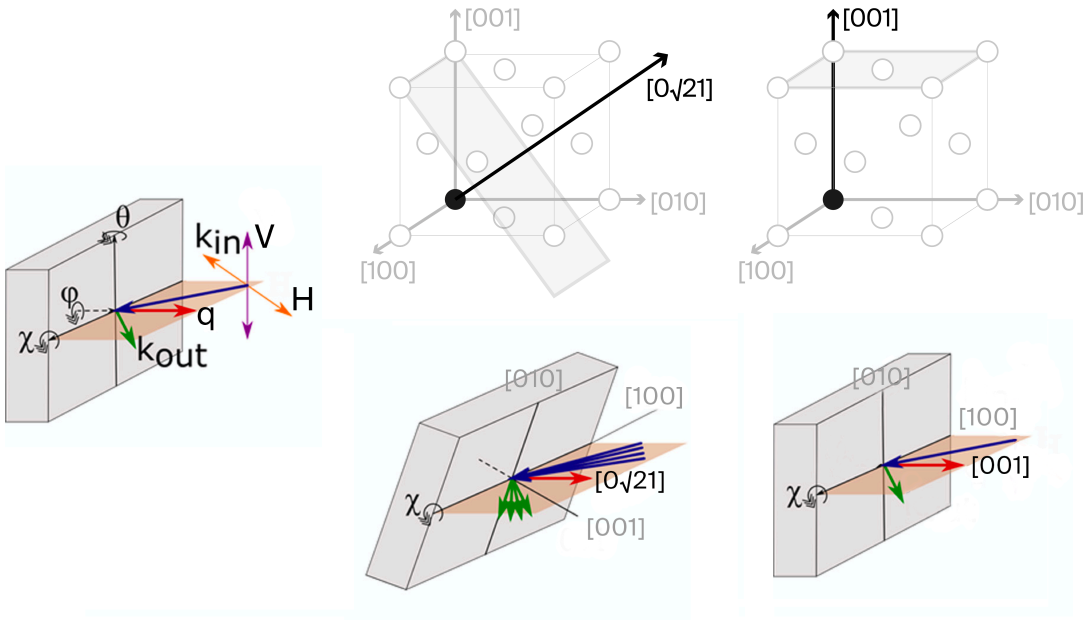

Figure 5.2: Sample geometry and scattering geometry for the [0√21] and [001] directions

The cobalt L_3 edge is at 780 eV, while for nickel the same edge is at 853 eV. This has consequences on the energy resolution of the measures of different materials: a cobalt elastic peak was measured to display a FWHM $\approx$ 30 meV while for nickel the value was slightly more, FWHM $\approx$ 37 meV.

5.2 Spectra Interpretation and Fitting

Before going to the result of the measurements, it is worth spending some time discussing the general shape of a RIXS spectrum to explain how it is obtained and the criteria used to interpret it. A single spectrum is made of many other spectra (scans): this is done to avoid photon double counting, allowing to use a centroid algorithm that applied to the CCD image increases the spatial resolution - and thus the energy resolution - of the technique. The scans are then aligned, as some drift can occur due to external factors, and summed. The resulting data is still in function of position: pixels are translated to electronvolts by a conversion factor that is determined experimentally. To find the energy zero the elastic peak is used, as discussed in the next section. The whole process involves both algorithmic and manual procedures and is done with "RIXSToolBox", a dedicated program for RIXS data processing developed by Kummer et al. as described in ref. [78].

After these steps, a typical RIXS spectrum looks like this:

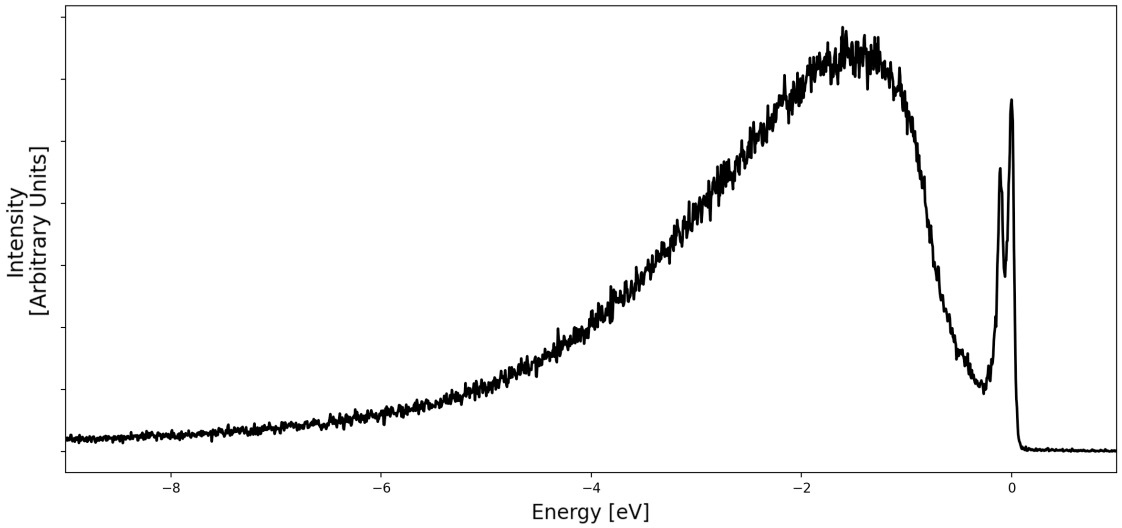

Figure 5.3: RIXS for a cobalt sample at q = 0.6 Å^{-1}, that will be discussed later.

The first obvious feature we observe is the large fluorescent peak centered at around 1.5 eV for cobalt and 0.8 eV for nickel. This broad figure is often present in RIXS spectroscopy but is exceptionally large in the case of metallic systems due to the presence of the valence band. For our purposes, no useful information is present in it, but it will be used in our case as a reference as it is known to not disperse or change shape with momentum. For this reason, its area can be used to normalize the intensity of each spectra.

What is interesting to us happens at low energies (in the 500 meV range), we are of course not interested in modelling the whole fluorescence shape. We want to use a curve that gives a good approximation of the fluorescence peak to treat it as a background, and we'll look at low energies only. This can be done in various ways, but our case showed that no big difference in the final results emerged by choosing one or the other. The most obvious approximation is to just use a linear function, or, better, a quadratic one [79, 69, 22]:

$$I_F(E) = (a_F E + bE^2) \cdot H(-E) \tag{5.1}$$

where $H(E)$ is the Heaviside step function and a_F and b are the free parameters. Another alternative, which is often found in literature, is to approximate to an exponential-like function:

$$I_F(E) = a_F \cdot e^{-bE} \cdot H(-E) \tag{5.2}$$

However, as here the Heaviside function is present as a sharp discontinuity with a given height a_F, with little physical sense, it is smoothed by convoluting the step-like part with a Gaussian with a width given by the instrumental resolution. This model is similar to what is used in ref. [80, 69, 22].

$$I_F(E) = a_F \cdot e^{-bE} \cdot \left(1 - \texttt{erf}\left(\frac{E}{\sqrt{2}\sigma_I}\right)\right) \tag{5.3}$$

Here σ_I is the instrumental resolution, `erf` is the error function and a_F and b are again free parameters.

Differently from a Colbalt spectrum like in fig. 5.3, fluorescence in nickel is much closer to the elastic peak, and can potentially hide interesting low energy excitations. As it is customary in RIXS measurements [22], a way to avoid this problem is, in principle, to detune the energy above the absorption edge: due to its nature fluorescence is known to shift downward when energy is increased. In this case, nickel detuning was 1 eV.

The procedure, that was already tried in the previous work by the same group [22], is based on the assumption that the spin wave spectra is not affected by detuning. For this reason, both on and off resonance measures were taken in the RIXS spectra of nickel (see fig. 5.4).

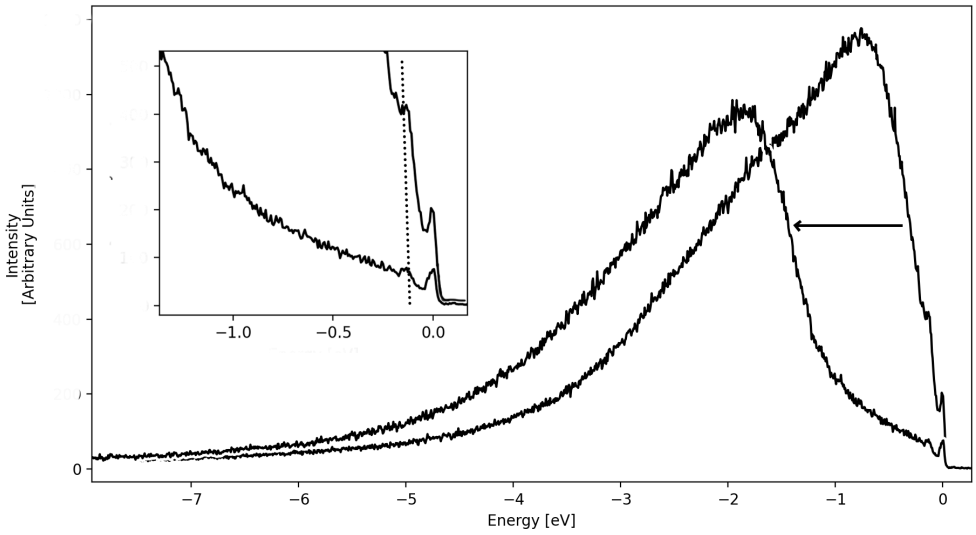

Figure 5.4: Effects of detuning on the final spectra. These nickel measurements, discussed later, were taken after shifting the incoming energy from 852 eV to 853 eV. The inset is a zoom of the low energy region, where a spin wave is present both on and off resonance in the same position.

The other clear element is the intense peak positioned at E = 0 eV, which is of elastic nature. This is almost always visible, but has a strong dependence on the scattering angle. It is not good as a reference for intensity, but it is useful to find the energy zero of the whole spectra. As discussed in the previous section, recall that for statistical reasons many spectra are acquired and their alignment before averaging is based on the position of this peak, as it is both visible and unique.

In our fitting, we'll model the elastic peak as a Gaussian with its width limited by instrumental resolution.

$$I_E(E) = a_E \cdot \frac{1}{\sigma_I \sqrt{2\pi}} \cdot e^{-\frac{1}{2}\frac{(E-E_0)^2}{{\sigma_I}^2}} \tag{5.4}$$

σ_I is the instrumental resolution, E_0 is the energy zero which might not exactly coincide with the one found by eye during the energy conversion. a_E is a free parameter.

The second peak at finite energy loss is in the position where we expect a spin wave collective excitation. Various options exist for its fitting. In our case, we decided to use the equation of the damped oscillator [81]:

$$I_{SW}(E,\mathbf{q}) = \frac{a_{SW}\cdot E}{\left(E^2 - E(\mathbf{q})^2\right)^2 + E^2 s^2}\cdot\frac{1}{1-e^{-\beta E}} \tag{5.5}$$

Finally, $E(\mathbf{q})$ is the spin wave dispersion we are looking for, and thus appears as a parameter for each spectrum and fit. $\beta = 1/k_B T$ is simply the Boltzmann factor, while a_{SW} and s are free parameters of the model as well. Temperature was taken to be the one of the measurements, 20 K. The particularity of this curve is that the peak position is not actually corresponding to the exact position of the magnetic excitation.

It might happen that the three functions described just above are not enough to replicate the measured spectrum with accuracy. Usually, some spectral intensity seems to be leftover in the in-between region from the spin wave to the elastic peak. As this region is usually the one where phonons are expected [57], their presence is accounted for by a second Gaussian. Although many phonon branches usually exist, and many of them are not visible to each RIXS configuration, the use of this last function is of semi-euristic nature. It is usually considered sufficient to use a single peak in a reasonable energy window and to limit its width to the one of the instrumental resolution.

$$I_P(E,\mathbf{q}) = a_P\cdot\frac{1}{\sigma_I\sqrt{2\pi}}\cdot e^{-\frac{1}{2}\frac{(E-E_P(\mathbf{q}))^2}{{\sigma_I}^2}} \tag{5.6}$$

Here, a part from a_P, the other parameter is the position of the Gaussian which is of course dispersing as $E_P(\mathbf{q})$.

At the end, data for each spectrum was fitted with an equation:

$$I(E) = I_F(E) + I_{SW}(E,\mathbf{q}) + I_E(E) + I_P(E,\mathbf{q}) \tag{5.7}$$

σ_I, which appears in many of the functions considered, is not strictly fixed to the resolution of the instrument, but it is left as free to be slightly higher to account for possible resolution degradation due to drift or external factors.

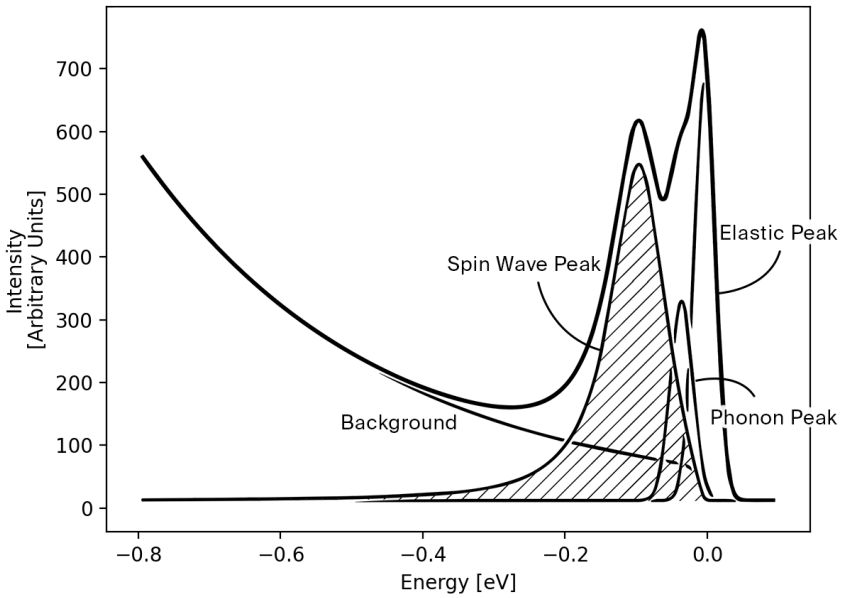

Figure 5.5: An example of the fitting function. The spin wave peak is shaded in this graph for clarity.

It shall be noted that the spin wave peak is not always as clear as in the case above. The way in which we worked was to put constraints to let each component behave in a physically "reasonable" way.

5.3 Cobalt

As we already mentioned in section 4.3, two different cobalt samples were prepared and succesfully measured.

The first one was measured along the [0$\sqrt{}$21] and [001] directions, while the second was just measured along [0$\sqrt{}$21] only to verify reproducibility of the previous results. We'll display the results together, but we'll highlight from which set of measures each comes from.

[0$\sqrt{}$21] Direction

For the first 7 nm cobalt sample, eight spectra were taken, each of 100 scans of 45 seconds. The q values were chosen to be inside the extremes of the instrument window, which is dictated by the physical angular range of the spectrometer arm. These values are q = 0.348 Å^{-1} and q = 0.763 Å^{-1}. These spectra already showed a very clear dispersion of the spin wave peak, which is most of the times clearly visible.

The second 7nm cobalt sample, prepared in the same manner at a time distance of three months, was measured at new values of q for a total of six spectra.

It is important to notice, as it seems not be the case for nickel, that although measurements took place over a long time of more than 24 hours, no contamination or degradation seems to have taken place.

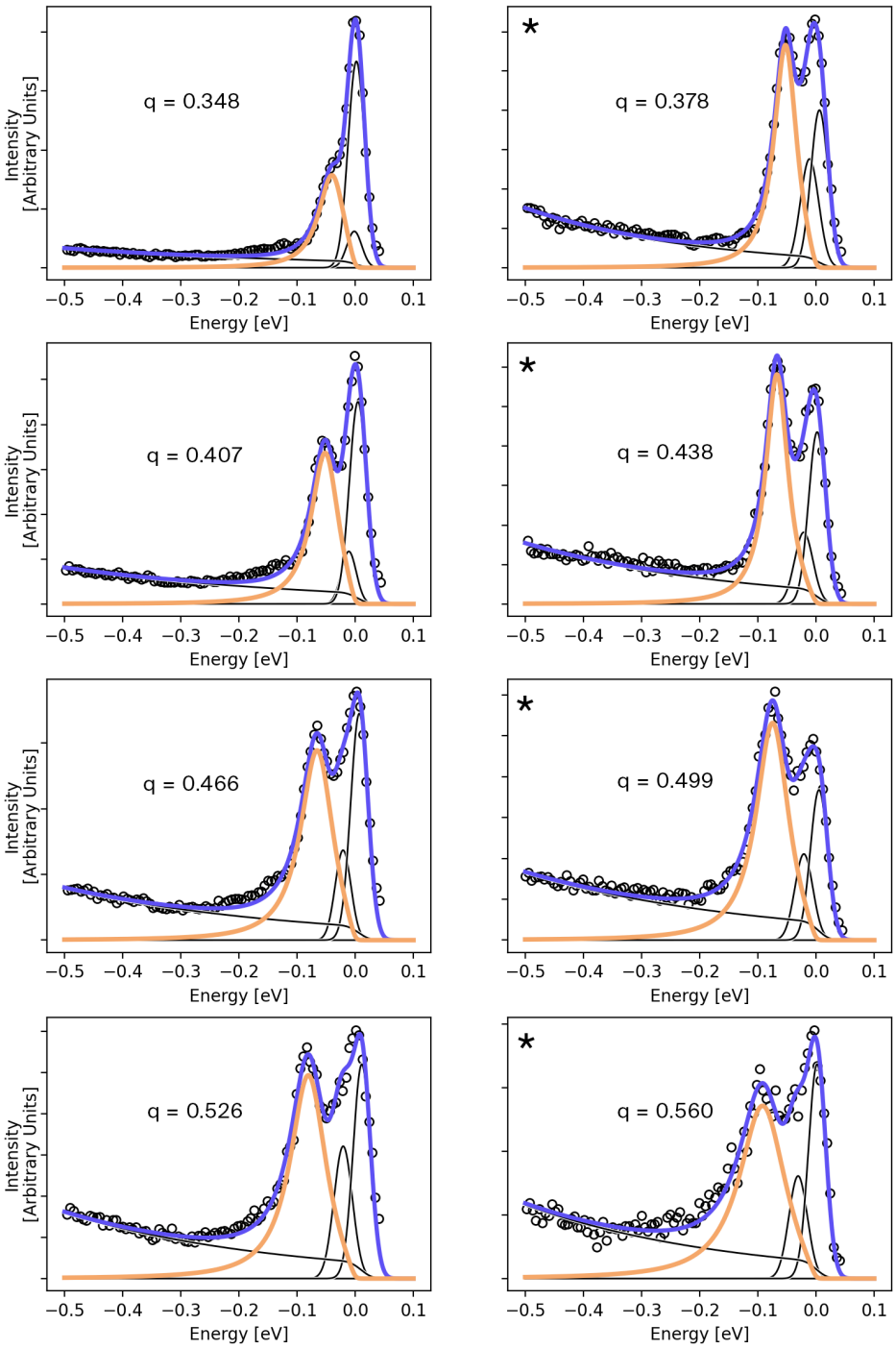

(continues in the following page)

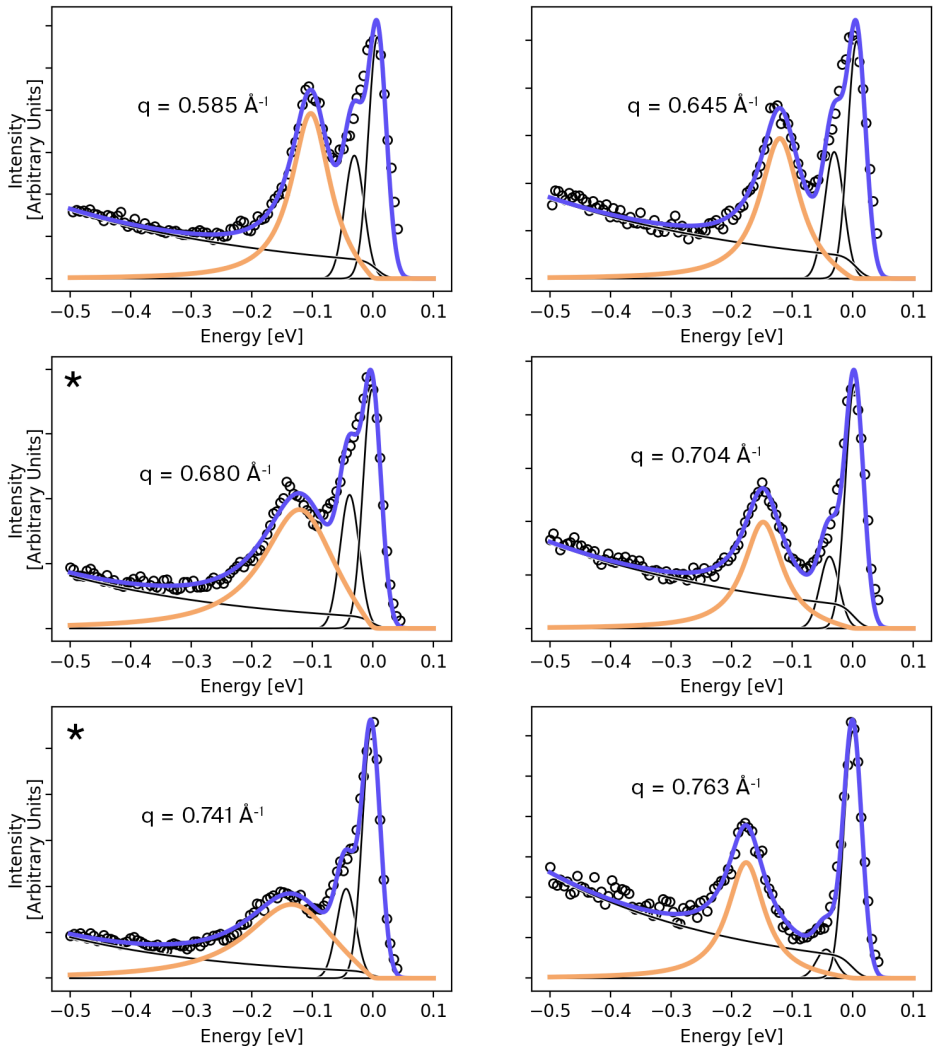

Figure 5.6: Cobalt [0$\sqrt{21}$] RIXS spectra at different q. The spin wave contribution is shown in orange. Starred spectra are from the second set of measurements.

For the fits, the exponential-like background was used as well as a phonon with Gaussian shape, as discussed in the previous section. The energy range of this last phonon, that ideally takes care of more than one possible branch, never exceeds the 40 meV range. This is in partial agreement with theoretical and experimental results [82, 83], where the value for our q values is of around 20-30 meV.

With the fitting done, we can finally look at the q dependence of the spin wave energy peak position, and try to model its dispersion with our available knowledge. Notice that half of the points from the second set of measurements agrees with the others, the two main exceptions being the high q points, for which the peak width in fig. 5.6 seems to have gotten broader. The reason of this is currently not known.

For fitting the dispersion in order to find the value of the stiffness constant, the first choice is to try the simplest form possible, namely the quadratic equation $E(q) = Dq^2$. From this, we can directly find a value for D, which we can compare with literature. As the curve doesn't

seem to perfectly fit our data, we also try to use the full, non-approximate form of eq. (2.8). As seen in fig. 2.5, the region we are working in should be one in which the approximation start to be less valid. Here, D is not present in its explicit form, but can be obtained easily from the product JS. Recall that no direct justification for the use of this expression in metals yet exists, but the curve seems to fit our points slightly better nevertheless.

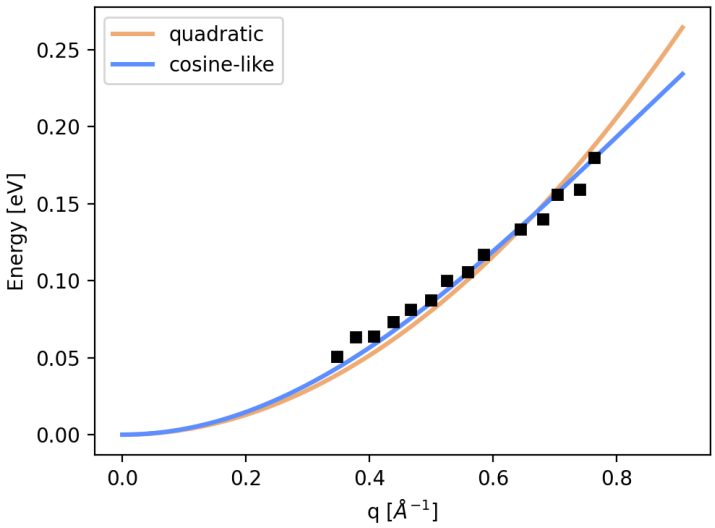

Figure 5.7: Spin wave peak positions for the cobalt [0$\sqrt{21}$] data. Error bars are smaller than marker size.

The values obtained for the stiffness in this case are $D = 321 \pm 8$ meV Å^2 for the quadratic dispersion and $D = 372 \pm 6$ meV Å^2 for the cosine-like one.

[001] Direction

Fewer measurements were taken along the [001] direction: The reason we focused on the other direction for cobalt is that here the elastic contribution is much higher than in the [0$\sqrt{21}$] direction, and it could mask the peaks of interest. In fact, to reduce its intensity we detuned χ by a few degrees (3-5°), with little overall effect on the measured q direction. With this tweak, although the peak is still very high, the spin wave dispersion is almost always visible. Six spectra were acquired at the q shown in fig. 5.8, each based on 130 scans of 45 seconds. Here the dispersion window is slightly different, and goes from q = 0.348 Å^{-1} to q = 0.774 Å^{-1}. The fitting is performed as in the previous case and shown hereafter.

The dispersion fit follows the same procedure as before, with the difference that here we'll be using eq. (2.7) as cosine-like function to fit the data to instead of eq. (2.8). The same qualitative remarks can be done. We can see that the first point of the dispersion has remarkably high error bars: this is simply due to the presence of the phonon and the high elastic peak, that make it difficult to fit a spin wave peak. A part from this detail, the data is well-fitted, and we obtain the values of $D = 332 \pm 8$ meV Å^2 for the quadratic dispersion and $D = 377 \pm 4$ meV Å^2 for the cosine-like function.

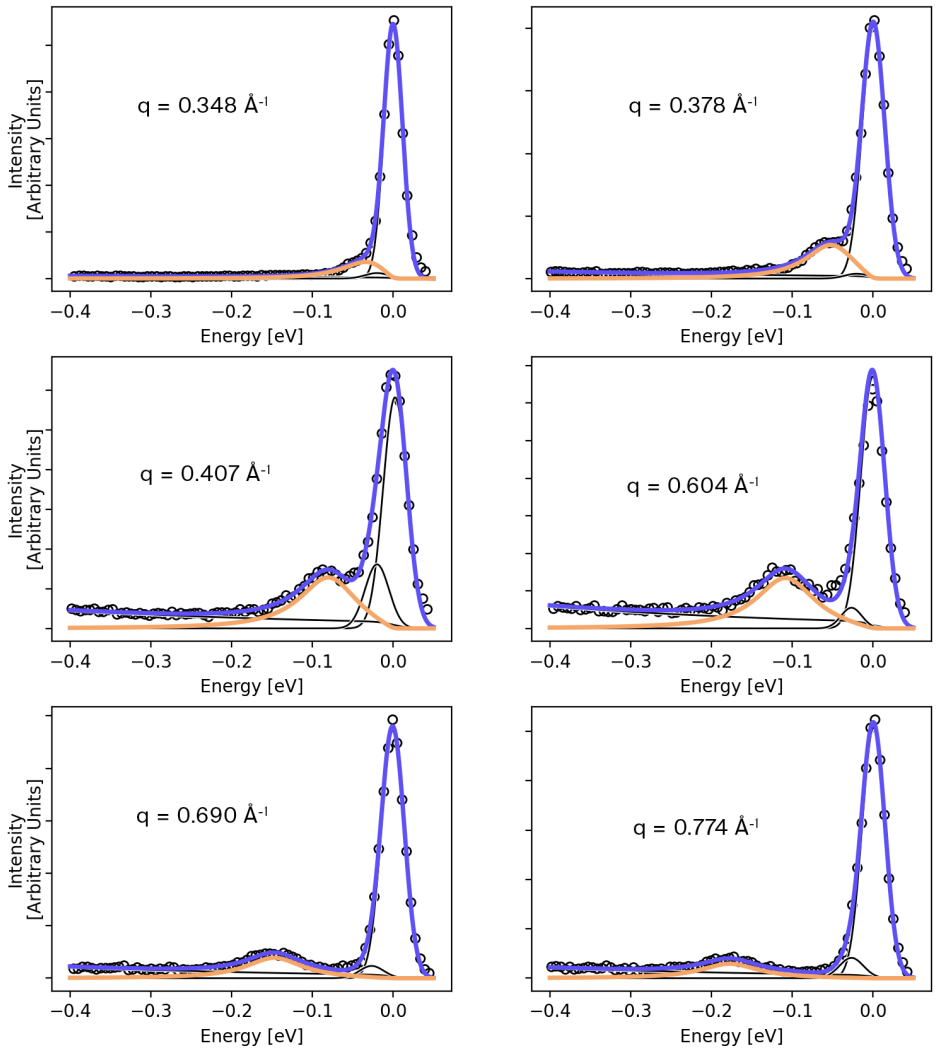

Figure 5.8: Cobalt [001] RIXS spectra at six different q. The spin wave contribution is shown in orange.

The fact that the stiffness values found in the two directions are close enough to be considered the same is not surprising, as it has been already discussed in chapter 2. It would be useful to understand which of the two fitting equations is more accurately describes the data. The second fit, with the cosine-like function found in the nearest neighbour Heisenberg model of chapter 2, seems to give a more tight fit by eye. The variance found for the cosine-like fits is also slightly better than with the quadratic dispersion, even if not by much, and the final values of D are closer to each other. A more interesting and complete way to answer this question however is comparing the value with data from other measurements.

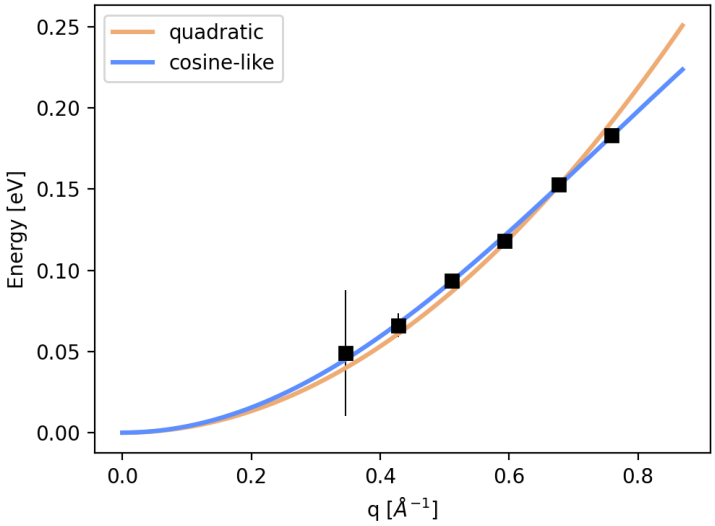

Figure 5.9: Fits for the cobalt [001] data. When not shown, error bars are smaller than marker size.

Comparison with previous experiments and calculations

As we have previously stated, the main tool for studying spin waves has historically been Inelastic Neutron Scattering. The need of macroscopic samples makes measuring fcc cobalt hard, as this it is not a thermodinamically favoured configuration at ambient temperature. In this sense, fcc cobalt has never been directly measured by INS as it was always some form of alloy, stable at ambient temperature. Nevertheless, the 1960 results of ref. [11] perfecty agrees with our data, even if the fcc cobalt sample contained Iron to an extent of 8%. For what regards hcp cobalt, old measures seemed to hint to higher values of around 490 meV Å^2 [12], while more recent ones [13] point to lower values which are closer to our fcc case.

Another technique able to capture spin waves in thin films with good resolution is Spin Polarized Electron Energy Loss Spectroscopy (SPEELS). Measures on 8 ML (1.5 nm) samples of fcc cobalt were performed and showed values which are reasonably close to ours [84, 85]. In ref. [84] the lower value of around 340 meV Å^2 with respect to previous INS and Brillouin Light Scattering experiments [86] is justified by the use of a thin film instead of a bulk sample. A RIXS thickness dependent study of D, as done in ref. [23], might help settling this point as the measures of ref. [85], although less recent, are in agreement with both ours and those for the fcc cobalt alloy.

In the end, looking at the totality of available data, it is reasonable to assume that our fit that employs the non-approximated form of the spin wave dispersion is more correct, as it agrees pretty well with most of the previous literature.

Ab initio calculations have been performed as well, as for example in ref. [87], showing that theoretical models, if compared with a large set of experiments, don't seem to be capable of reproducing the spin wave spectra effectively.

These results are grouped in the following table in chronological order.

Table 5.1: Recap table of previous results from literature along with ours, averaged.

System	Method	year	D [meV Å^2]
fcc Co 8% Fe [11]	INS	1960	381 ± 39
hcp Co [12]	INS	1966	490 ± 20
hcp Co [13]	INS	1995	412 ± 12
fcc Co [86]	BLS	1996	466 ± 16
fcc Co [87]	calc.	2001	663 ± 6
fcc Co 8ML [85]	SPEELS	2003	388 ± 3
fcc Co 8ML [84]	SPEELS	2012	346 ± 14
fcc Co 7nm	RIXS	2021	375 ± 4

Some additional calculations were done by Kun Cao of Sun Yat-sen Univerisity using LDA, in a similar way to what was done in refs. [22, 24] and based on the framework of Melnikov [2]. The chosen directions were the ones originally intended for measure, [001] and [111]. The first thing we observe is that, in line with previous calculations of ref [87], the stiffness D is higher than that of experimental data as its value ranges from 450 meV Å^2 in the quadratic approximation to 525 meV Å^2 in the cosine-like fit (fig. 5.10).

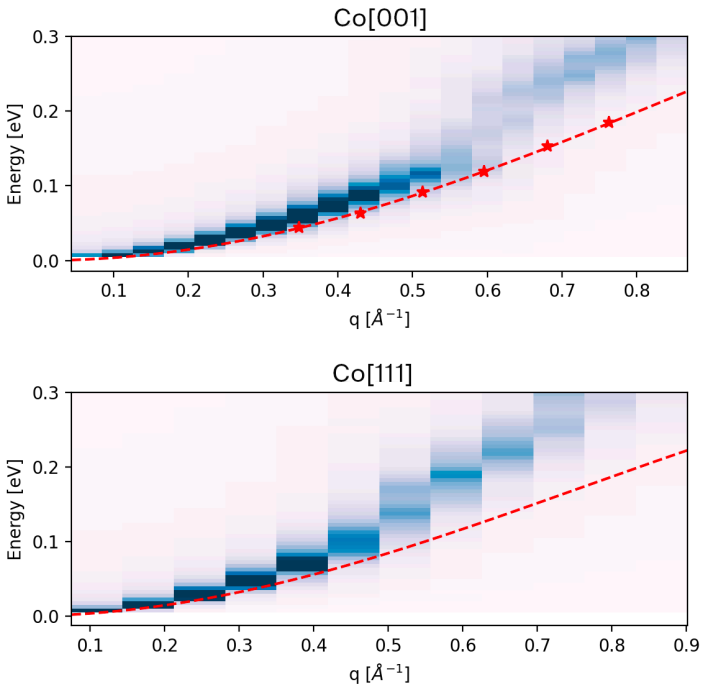

Figure 5.10: The calculated dispersions for the [001] and [111] Directions of fcc cobalt. The red dotted line is calculated with the stiffness found from experiments. The red stars in the [001] plot are in correspondence of our measures.

We can directly compare the [001] simulations with our measures, where some additional differences arise. If we try to look at the shape of the peaks, which should reproduce the one of experiments, a strongly damped region is observed between around q = 0.6 Å^{-1} and q =

0.7 Å^{-1}. Recall that the FWHM of the magnon peaks might contain information about an eventual interaction with the Stoner continuum, as explained in chapter 2: this phenomena is not observed at all in our measures, and is also absent in the [0,√21] direction calculations, where the widths decrease steadily. Apart from the described region, the FWHM is of comparable magnitude if we consider the effect of instrumental resolution. Qualitatively, the peak height and area show comparable behaviour despite the discussed region.

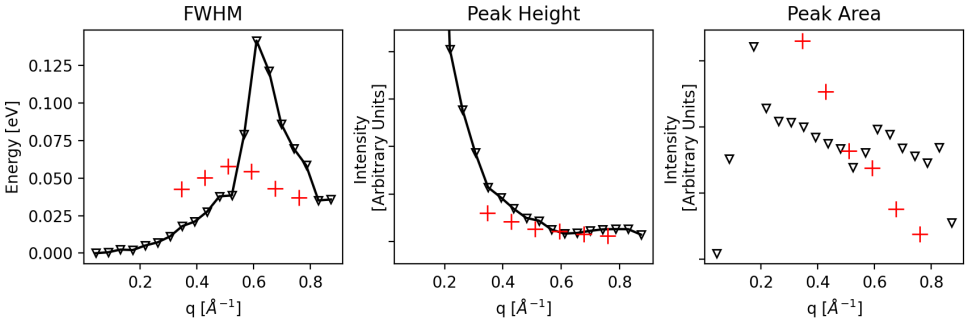

Figure 5.11: [001] Direct comparison. Black triangles are from *ab initio* calculations. Red crosses are from our fits, and their FWHM is deconvoluted with instrumental resolution after approximating the peak shape to that of a Lorenzian. Peak intensity of our measures is adjusted to be in the same window of the calcualations.

5.4 Nickel

Measuring nickel proved itself to be harder than expected. The first problem was described through the rest of this work, and we'll adddress it fully now. As the first sample of 5nm, which displayed strong out of plane magnetization (see fig. 4.15), was measured, no spin waves where observed either on and off-resonance. The geometric cross section of RIXS scattering for spin waves was then studied by numerical methods to ensure that their eventual absence for this case was of physical nature.

Calculations were performed by Davide Betto using Quanty code [88] with the two symmetric directions of magnetization, in-plane and out-of-plane, as described in [22]. Although the calculations were performed for measures along the [111] direction, which was the one originally intended, the result should have little difference as we are just performing an in-plane rotation of 45° degrees and the symmetry of either magnetization configuration remains the same. The result shows the possibility of being partially unable to see spin waves if the magnetization direction of the sample is out of plane.

As it can be seen in fig. 5.12 the in-plane magnetization gives nonzero cross section for all wavevectors. On the contrary, for out-of-plane magnetization, a region of finite but low cross section is present at the same wavevectors as our measurement. This justifies what has been carried out throughout section 4.3: no clear spin-wave presence was observed in either of the samples that displayed out-of-plane magnetizations, those of 10 and 15 nm (see fig. 4.16 and fig. 4.17).

Finally, when a cobalt buffer layer was grown before nickel as suggested in ref [76] a distinct peak was immediately seen along with in-plane magnetization, as can be seen clearly in fig. 5.13).

When this problem was solved, only a handful of measures were taken for reasons of time. The

[0$\sqrt{21}$] direction was chosen and a total of eight spectra of 300 scans of 40 second each were taken. The last two spectra (see fig. 5.14) have a lower number of scans due to less available time.

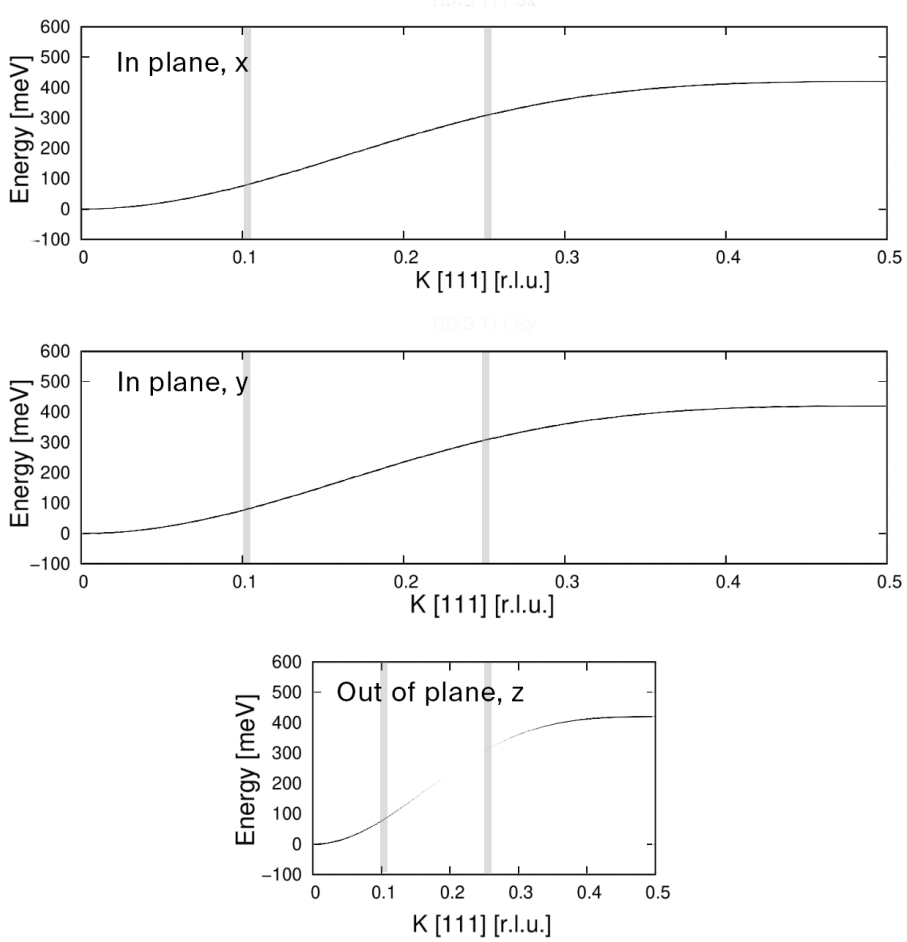

Figure 5.12: Cross section of in-plane and out-of-plane magnetization as a function of wavevector and energy. The interval of our measurements is delimited by gray bars.

To make sure that the anomalous behaviour of ref. [22], where a flattening of the dispersion takes place, was not effected by the detuning of the incident energy, the very first measurement was performed both on-resonance and off-resonance, on a q point that did show discrepancies between previous RIXS and INS studies. As it is shown in fig. 5.4 and more closely in fig. 5.13 and fig. 5.14 (spectra 1 and 2), a spin wave peak is clearly present in both. If compared with previous data from [22], its energy value is higher and seems to be more comparable with some of the previous INS measurements [9]. As detuning decreases intensity (see eq. (3.6), where the energy difference appears at the denominator), a first set of four measurements was performed on resonance. Although the first peak was promising, two peaks at higher momenta were mostly buried in the background. A point at low q was taken as well and reproduced the previous results, more in agreement with INS than with previous RIXS.

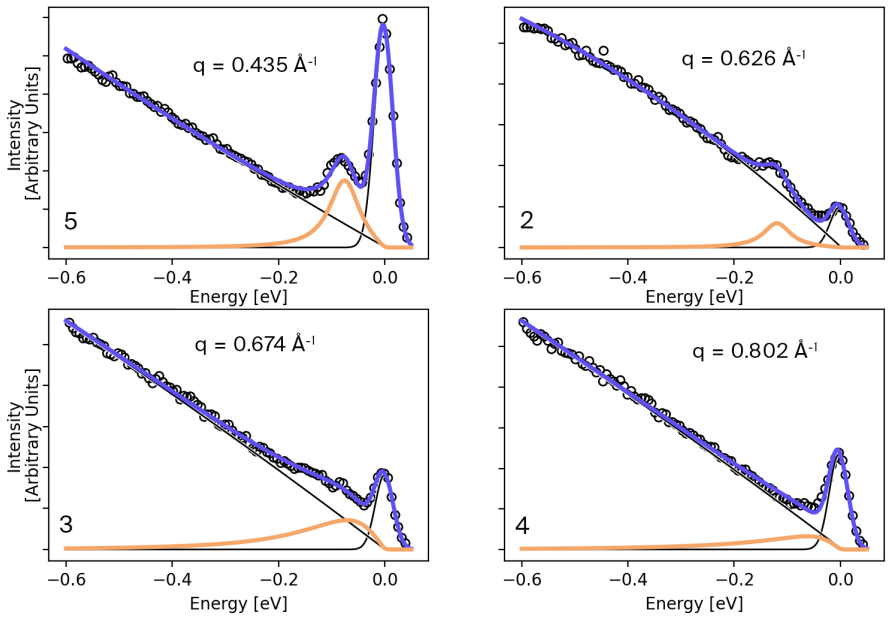

Figure 5.13: On-resonance nickel [0$\sqrt{21}$] RIXS spectra at four different q. The spin wave contribution is shown in orange. Bottom left number indicates the order in which the spectra were taken (see also fig. 5.14).

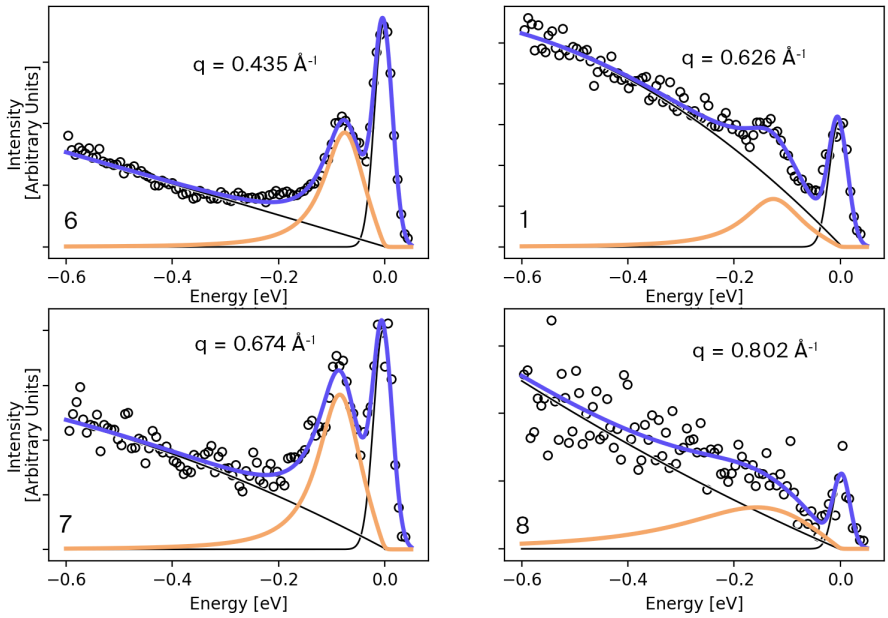

Figure 5.14: Off-resonance nickel [0$\sqrt{21}$] RIXS spectra at four different q. The spin wave contribution is shown in orange. Bottom left number indicates the order in which the spectra were taken (see also fig. 5.13).

As we were interested in the dispersion at high q, where we wanted to investigate the nature of the anomalous flattening observed for bulk nickel, we repeated the measures for the two high momenta points also off-resonance.

Here the second problem of measuring nickel took place, as coming back to them the positions of the peak shifted downwards in the off-resonance measurements, in a similar way to what happened in ref. [22]. However, the fact that the point at q = 0.626 Å^{-1} was initially well above those measurements, hints to the fact that this energy change should not be an effect of resonance. As the effect took place only after hours of measurements, the suggested explanation is that the energy deviation might be related to contamination effects, and thus appear only after long measuring times. The reasons why contamination should directly affect spin waves and their dispersions is still unclear. Nevertheless, the final XAS for the examined point showed a shoulder on the L_2 peak (see fig. 5.17).

In the following figure we plot our data along with the one from ref. [22]. Only three out of four q points are shown for our measurements as for the highest q value it was impossible to extrapolate a clear spin wave peak. Data, especially that taken at early times, agrees fairly well with previous neutron measures like the ones from ref. [9]. It is interesting to notice that older neutron data by the same author does indeed show a situation in which the peaks are shifting from the usual spin wave dispersion [10], similarly to what happens in RIXS. Fitting was performed using the quadratic background and without considering any phonon.

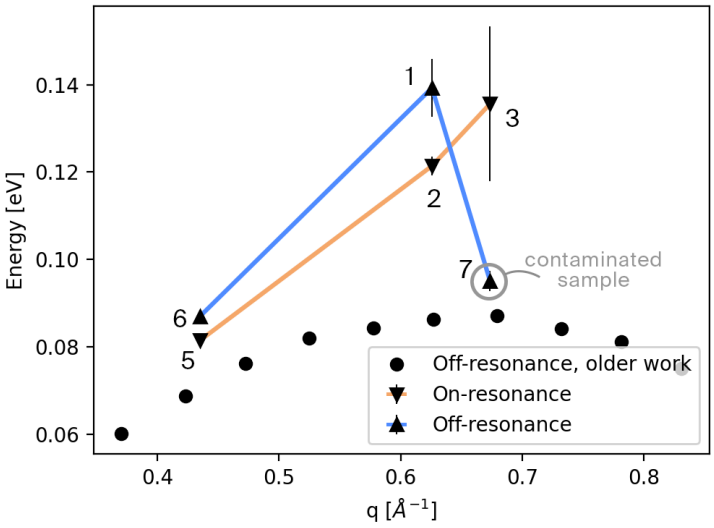

Figure 5.15: Extrapolated peak position for spin waves in the on-resonance and off-resonance spectra. Data from previous measures [22] is displayed as well.

A more in depth study, like the one performed for cobalt, is necessary. However, we can nevertheless compare our data with some *ab initio* calculations of the same kind of those described in the previous section, even if the results are for a different direction. We can intuitively see that, even if optimistically we take the on-resonance measures as good, the dispersion they hint to is yet again well below the calculated one, meaning the stiffness constant D will surely be lower than the one estimated numerically, in a similar manner to what happens

for cobalt. For what concerns the widths, calculations show an increasing FWHM but no sharp transition to an eventual Stoner region. However, we have too few data to compare this with our measurements.

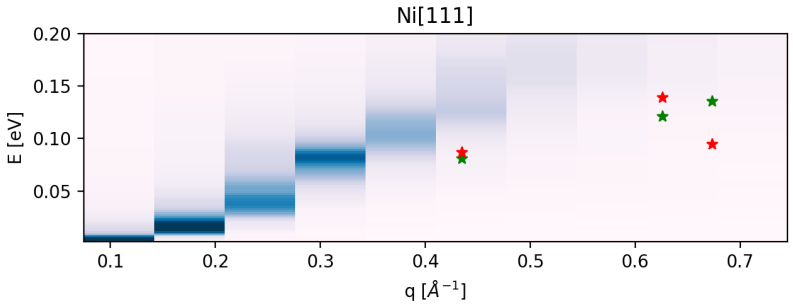

Figure 5.16: Comparison of *ab initio* calculations for nickel spin waves in the [111] direction compared with the peak positions of our measures in the $[0\sqrt{21}]$ direction. Green stars are on-resonance while Red stars are off-resonance.

A more consistent study of nickel is required, but the information acquired on the importance of magnetization direction and on the possibility to detune without fear to affect the dispersion are promising. A solution for the possible contamination should be tested in future experiments.

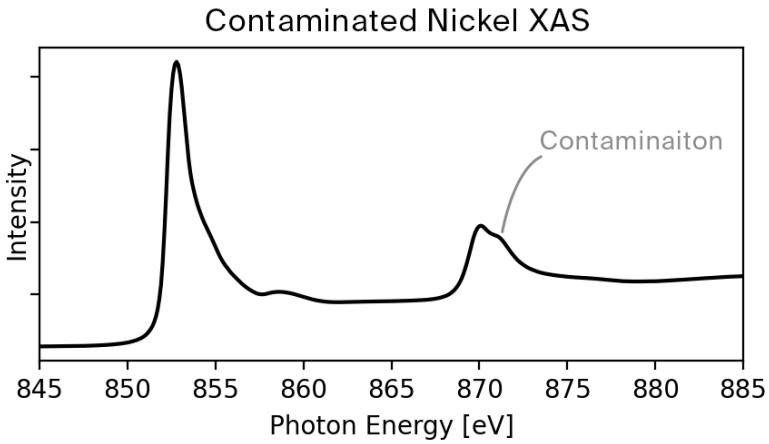

Figure 5.17: XAS of the 7 nm nickel sample with the 1 nm cobalt buffer layer. The shoulder on the L_2 peak is sign of contamination and was not present in the beginning.

Chapter 6

Conclusions and Outlook

In this Thesis, a RIXS study of two 3d ferromagnetic metals has been carried out, namely of fcc cobalt and nickel.

Measurements of fcc cobalt were successful: the result is reproducible to a good extent and in good agreement with data from previous experiments carried out with other techniques such as INS and SPEELS . We recall that our choice of fcc cobalt reflects our initial premise to try and understand if the differences between iron and nickel from ref. [22] could be explained by means of an electronically in-between case. The dispersion in our measures is clear and does not seem to have any sort of deviation, as happens with nickel. However, just as in nickel, the energies are overestimated by calculations: these discrepancies make us think that correlation effects might not be the only missing piece of the many body problem modelled by *ab initio* calculations.

To give a more consistent look to the whole study, and to understand better to which extent the extrapolated values of D are influenced by the dimensions of the sample, a thickness dependent RIXS study like the one of Pelliciari et al. [23] could be carried out. To test the effect of possible distortions of the lattice on the stiffness, new calculations and more direction dependent measurements could also be performed.

For nickel, some forward steps were made but we are still not answering all the questions we had in the beginning. We established the importance of the direction of magnetization in the sample also experimentally, and we seem to have shown that detuning the incoming energy above the edge should not affect the measurements of the spin wave position. If it is needed, this last assumption can also better be tested with a sample of cobalt or iron, by performing a series of measurements on and off-resonance for high momenta on what is now a more or less consolidated dispersion.

What still remains unanswered is the energy deviation that happens at high q. Its apparent dependence on time and the final XAS suggest a problem of contamination. Nickel seems to be much more sensitive to contamination than iron and cobalt. This was not apriori expected. At the same time, although it is known that contamination can effect the magnetisation of a ferromagnetic system, why spin wave positions change is again not clear.

We feel that with the acquired knowledge, some extra trials should be made to understand better the problem of the shifting dispersion, and to evaluate the possibility of it coming from the interaction with the Stoner continuum. Growing a capping layer, of either copper or cobalt, to protect the sample from contamination is surely the next thing to be tried, and should be reasonably feasible due to the powerful chemical sensitivity of RIXS and to the flexibility of

MBE.

The two experiments have shown that RIXS can give good results for the measurement of spin waves in metallic systems. For the future, especially after the study of nickel is eventually perfectioned, one possibility is to try to employ epitaxial growth to its full, designing alloy films, performing systematic studies on different phases of the same material, growing sandwiches and multilayers, or even designing nanometric or mesoscopic systems.

It shall be noted that, during the preparation of the experiments of this work, a sample of this kind was already tested: a cobalt film covered by a 12ML wedge of copper was measured in RIXS to look for Quantum Well States [89, 90, 91]. Although the result was negative, both XAS and RIXS showed that the technical possibility is mature enough to be employed.

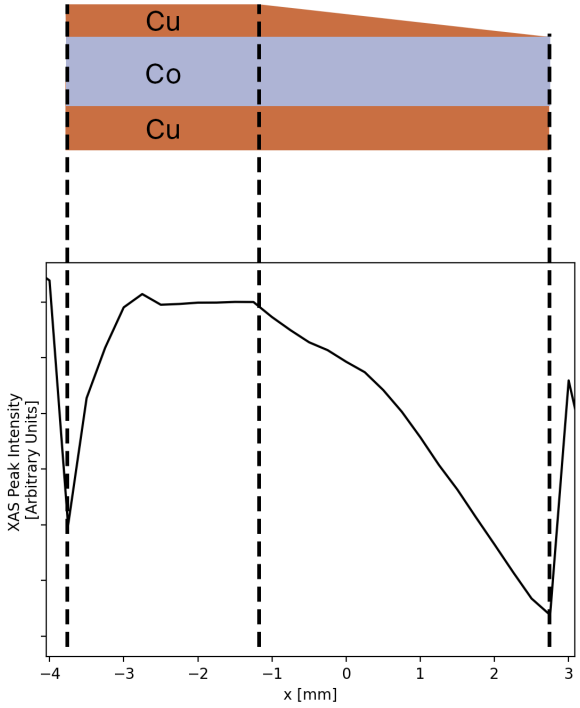

Figure 6.1: Scheme of the 12 ML copper wedge grown on 7 nm fcc cobalt. Below, the L_3 XAS peak on the copper edge is shown in function of position. Aside from the two sample sides, that give a dip, we can see a clear flat region (on the left) and a steadily decreasing one (on the right), showing the wedge growth was successful.

Bibliography

[1] S Blundell. *Magnetism in Condensed Matter*. Oxford Master Series in Condensed Matter Physics. OUP Oxford, 2001. ISBN: 9780198505914. URL: https://books.google.fr/books?id=OGhGmgEACAAJ.

[2] Nikolai B Melnikov. *Dynamic Spin Fluctuation Theory of Metallic Magnetism*. Springer, 2018.

[3] J Kübler. *Theory of itinerant electron magnetism*. Vol. 106. Oxford University Press, 2017.

[4] E Şaşıoğlu et al. "Wannier-function approach to spin excitations in solids". In: *Physical Review B* 81.5 (2010), p. 054434.

[5] BN Brockhouse. "Scattering of neutrons by spin waves in magnetite". In: *Physical Review* 106.5 (1957), p. 859.

[6] Gordon Leslie Squires. *Introduction to the theory of thermal neutron scattering*. Courier Corporation, 1996.

[7] EJ Samuelsen, MT Hutchings, and G Shirane. "Inelastic neutron scattering investigation of spin waves and magnetic interactions in Cr_2O_3". In: *Physica* 48.1 (1970), pp. 13–42.

[8] EJ Samuelsen and G Shirane. "Inelastic neutron scattering investigation of spin waves and magnetic interactions in α-Fe_2O_3". In: *physica status solidi (b)* 42.1 (1970), pp. 241–256.

[9] HA Mook and D McK Paul. "Neutron-scattering measurement of the spin-wave spectra for nickel". In: *Physical review letters* 54.3 (1985), p. 227.

[10] HA Mook and D Tocchetti. "Neutron-scattering measurements of the generalized susceptibility χ (q, e) for Ni". In: *Physical Review Letters* 43.27 (1979), p. 2029.

[11] RN Sinclair and BN Brockhouse. "Dispersion relation for spin waves in a fcc cobalt alloy". In: *Physical Review* 120.5 (1960), p. 1638.

[12] HA Alperin et al. "Observation of the dispersion relation for spin waves in hexagonal cobalt". In: *Journal of Applied Physics* 37.3 (1966), pp. 1052–1053.

[13] TG Perring, AD Taylor, and GL Squires. "High-energy spin waves in hexagonal cobalt". In: *Physica B: Condensed Matter* 213 (1995), pp. 348–350.

[14] LJP Ament et al. "Resonant inelastic x-ray scattering studies of elementary excitations". In: *Reviews of Modern Physics* 83.2 (2011), p. 705.

[15] J Schlappa et al. "Spin–orbital separation in the quasi-one-dimensional Mott insulator Sr_2CuO_3". In: *Nature* 485.7396 (2012), pp. 82–85.

[16] L Braicovich et al. "Dispersion of magnetic excitations in the cuprate La_2CuO_4 and $CaCuO_2$ compounds measured using resonant x-ray scattering". In: *Physical review letters* 102.16 (2009), p. 167401.

[17] L Braicovich et al. "Magnetic Excitations and Phase Separation in the Underdoped $La_{2-x}Sr_xCuO_4$ Superconductor Measured by Resonant Inelastic X-Ray Scattering". In: *Phys. Rev. Lett.* 104 (7 Feb. 2010), p. 077002. DOI: 10.1103/PhysRevLett.104.077002. URL: https://link.aps.org/doi/10.1103/PhysRevLett.104.077002.

[18] *EBS*. URL: https://www.esrf.eu/about/upgrade.
[19] NB Brookes et al. "The beamline ID32 at the ESRF for soft X-ray high energy resolution resonant inelastic X-ray scattering and polarisation dependent X-ray absorption spectroscopy". In: *Nuclear Instruments and Methods in Physics Research Section A: Accelerators, Spectrometers, Detectors and Associated Equipment* 903 (2018), pp. 175–192.
[20] C Dallera et al. "Soft X-ray emission spectroscopy at ESRF beamline 26 based on a helical undulator". In: *Journal of synchrotron radiation* 3.5 (1996), pp. 231–238.
[21] G Ghiringhelli et al. "Long-range incommensurate charge fluctuations in (Y, Nd)$Ba_2Cu_3O_{6+x}$". In: *Science* 337.6096 (2012), pp. 821–825.
[22] NB Brookes et al. "Spin waves in metallic iron and nickel measured by soft x-ray resonant inelastic scattering". In: *Phys. Rev. B* 102 (6 Aug. 2020), p. 064412. DOI: 10.1103/PhysRevB.102.064412. URL: https://link.aps.org/doi/10.1103/PhysRevB.102.064412.
[23] J Pelliciari et al. "Tuning spin excitations in magnetic films by confinement". In: *Nature Materials* 20.2 (2021), pp. 188–193.
[24] Kun Cao et al. "Ab initio calculation of spin fluctuation spectra using time-dependent density functional perturbation theory, plane waves, and pseudopotentials". In: *Physical Review B* 97.2 (2018), p. 024420.
[25] G Ghiringhelli et al. "Low energy electronic excitations in the layered cuprates studied by copper L_3 resonant inelastic x-ray scattering". In: *Physical review letters* 92.11 (2004), p. 117406.
[26] V Bisogni et al. "Ground-state oxygen holes and the metal–insulator transition in the negative charge-transfer rare-earth nickelates". In: *Nature Communications* 7.1 (2016), pp. 1–8.
[27] Y Lu et al. "Site-selective probe of magnetic excitations in rare-earth nickelates using resonant inelastic x-ray scattering". In: *Physical Review X* 8.3 (2018), p. 031014.
[28] A Geondzhian et al. "Large Polarons as Key Quasiparticles in $SrTiO_3$ and $SrTiO_3$-Based Heterostructures". In: *Physical Review Letters* 125.12 (2020), p. 126401.
[29] F Bloch. "Zur theorie des ferromagnetismus". In: *Zeitschrift für Physik* 61.3-4 (1930), pp. 206–219.
[30] T Holstein and HL Primakoff. "Field dependence of the intrinsic domain magnetization of a ferromagnet". In: *Physical Review* 58.12 (1940), p. 1098.
[31] VL Safonov. *Nonequilibrium magnons: Theory, experiment and applications*. John Wiley & Sons, 2012.
[32] G Shirane, VJ Minkiewicz, and R Nathans. "Spin Waves in 3d Metals". In: *Journal of Applied Physics* 39.2 (1968), pp. 383–390.
[33] C Herring and C Kittel. "On the theory of spin waves in ferromagnetic media". In: *Physical Review* 81.5 (1951), p. 869.
[34] C Herring. "Energy of a bloch wall on the band picture. II. perturbation approach". In: *Physical Review* 87.1 (1952), p. 60.
[35] SN Kaul. "Phase Transitions and Finite Temperature Magnetism: Experiment and Analysis". In: *Handbook of Magnetism and Advanced Magnetic Materials* (2007).
[36] Q Niu and L Kleinman. "Spin-wave dynamics in real crystals". In: *Physical review letters* 80.10 (1998), p. 2205.
[37] P Marra. "Theoretical approach to direct resonant inelastic x-ray scattering on magnets and superconductors". In: *arXiv preprint arXiv:1605.03189* (2016).
[38] YV Nazarov and J Danon. *Advanced Quantum Mechanics: A Practical Guide*. Cambridge University Press, 2013.
[39] J Als-Nielsen and D McMorrow. *Elements of modern X-ray physics*. John Wiley & Sons, 2011.

[40] NB Brookes. "High-Resolution Soft X-ray Resonant Inelastic X-ray Scattering". In: Jan. 2020, pp. 2367–2390. ISBN: 978-3-030-23200-9. DOI: 10.1007/978-3-030-23201-6_75.
[41] *Resonant Inelastic X-Ray Scattering End Station at ID32*. URL: https://www.esrf.fr/home/UsersAndScience/Experiments/EMD/ID32/RIXS.html.
[42] *EBS Parameters*. URL: https://www.esrf.eu/home/UsersAndScience/Accelerators/ebs---extremely-brilliant-source/ebs-parameters.html.
[43] H Schulte-Schrepping et al. *Commissioning of the APPLE II undulator*. Tech. rep. Tech. Rep. 1, 2002.
[44] T Schmitt et al. "High-resolution resonant inelastic X-ray scattering with soft X-rays at the ADRESS beamline of the Swiss light source: Instrumental developments and scientific highlights". In: *Journal of Electron Spectroscopy and Related Phenomena* 188 (2013), pp. 38–46.
[45] GC Ghiringhelli et al. "SAXES, a high resolution spectrometer for resonant x-ray emission in the 400–1600 eV energy range". In: *Review of Scientific Instruments* 77.11 (2006), p. 113108.
[46] FMF De Groot, P Kuiper, and GA Sawatzky. "Local spin-flip spectral distribution obtained by resonant x-ray Raman scattering". In: *Physical Review B* 57.23 (1998), p. 14584.
[47] J van den Brink. "The theory of indirect resonant inelastic x-ray scattering on magnons". In: *EPL (Europhysics Letters)* 80.4 (2007), p. 47003.
[48] K Kummer et al. "The high-field magnet endstation for X-ray magnetic dichroism experiments at ESRF soft X-ray beamline ID32". In: *Journal of synchrotron radiation* 23.2 (2016), pp. 464–473.
[49] PFA Alkemade, WC Turkenburg, and WF Van Der Weg. "Initial growth of nickel on copper (100) studied by ion-scattering". In: *Nuclear Instruments and Methods in Physics Research Section B: Beam Interactions with Materials and Atoms* 15.1-6 (1986), pp. 126–129.
[50] S Müller et al. "Pseudomorphic growth of Ni films on Cu (001): a quantitative LEED analysis". In: *Surface science* 364.3 (1996), pp. 235–241.
[51] W Platow et al. "Structure of ultrathin Ni/Cu (001) films as a function of film thickness, temperature, and magnetic order". In: *Physical Review B* 59.19 (1999), p. 12641.
[52] JR Cerda et al. "Epitaxial growth of cobalt films on Cu (100): a crystallographic LEED determination". In: *Journal of Physics: Condensed Matter* 5.14 (1993), p. 2055.
[53] CM Schneider et al. "Curie temperature of ultrathin films of fcc-cobalt epitaxially grown on atomically flat Cu (100) surfaces". In: *Physical review letters* 64.9 (1990), p. 1059.
[54] MA VanHove, WH Weinberg, and C Chan. *Low-energy electron diffraction: experiment, theory and surface structure determination*. Vol. 6. Springer Science & Business Media, 2012.
[55] F Jona, JA Strozier Jr, and WS Yang. "Low-energy electron diffraction for surface structure analysis". In: *Reports on Progress in Physics* 45.5 (1982), p. 527.
[56] M Pl Seah and WA Dench. "Quantitative electron spectroscopy of surfaces: A standard data base for electron inelastic mean free paths in solids". In: *Surface and interface analysis* 1.1 (1979), pp. 2–11.
[57] A.N. W et al. *Solid State Physics*. HRW international editions. Holt, Rinehart and Winston, 1976. ISBN: 9780030839931. URL: https://books.google.it/books?id=oXIfAQAAMAAJ.
[58] O Hardouin Duparc. "Pierre Auger–Lise Meitner: comparative contributions to the Auger effect". In: *International journal of materials research* 100.9 (2009), pp. 1162–1166.
[59] DR Vij. *Handbook of applied solid state spectroscopy*. Springer Science & Business Media, 2007.

[60] JC Riviere. "Auger electron spectroscopy". In: *Contemporary Physics* 14.6 (1973), pp. 513–539.
[61] Lawrence E Davis et al. *Handbook of Auger Electron Spectroscopy: A Reference Book of Standard Data for Identification and Interpretation of Auger Electron Specteroscopy Data*. Physical Electronics Industries, Incorporated, 1976.
[62] R Gonzalez. "Synthesis and in-situ atomic oxygen erosion studies of space-survivable hybrid organic/inorganic polyhedral oligomeric silsesquioxane polymers [electronic resource] /". In: (Jan. 2002).
[63] P Zimmermann et al. "Modern X-ray spectroscopy: XAS and XES in the laboratory". In: *Coordination Chemistry Reviews* 423 (2020), p. 213466.
[64] J Stöhr. "Exploring the microscopic origin of magnetic anisotropies with X-ray magnetic circular dichroism (XMCD) spectroscopy". In: *Journal of Magnetism and Magnetic Materials* 200.1-3 (1999), pp. 470–497.
[65] WL O'Brien and BP Tonner. "Orbital and spin sum rules in x-ray magnetic circular dichroism". In: *Physical Review B* 50.17 (1994), p. 12672.
[66] CT Chen et al. "Experimental confirmation of the X-ray magnetic circular dichroism sum rules for iron and cobalt". In: *Physical review letters* 75.1 (1995), p. 152.
[67] C Piamonteze, P Miedema, and FMF De Groot. "Accuracy of the spin sum rule in XMCD for the transition-metal L edges from manganese to copper". In: *Physical Review B* 80.18 (2009), p. 184410.
[68] L Morresi. "Basics of Molecular Beam Epitaxy (MBE) technique". In: *Silicon Based Thin Film Sol. Cells, Bentham Science Publishers* (2013), pp. 81–107.
[69] F Huang et al. "Magnetism in the few-monolayers limit: A surface magneto-optic Kerr-effect study of the magnetic behavior of ultrathin films of Co, Ni, and Co-Ni alloys on Cu (100) and Cu (111)". In: *Physical Review B* 49.6 (1994), p. 3962.
[70] J Shen, J Giergiel, and J Kirschner. "Growth and morphology of Ni/Cu (100) ultrathin films: An in situ study using scanning tunneling microscopy". In: *Physical Review B* 52.11 (1995), p. 8454.
[71] WH King. "Piezoelectric Sorption Detector." In: *Analytical Chemistry* 36.9 (1964), pp. 1735–1739. DOI: 10.1021/ac60215a012. URL: https://doi.org/10.1021/ac60215a012.
[72] K Hermann. "Appendix E: Parameter tables of crystals". In: *Crystallography and Surface Structure* (2011), pp. 265–266.
[73] EA Fitzgerald. "Dislocations in strained-layer epitaxy: theory, experiment, and applications". In: *Materials science reports* 7.3 (1991), pp. 87–142.
[74] JW Matthews and JL Crawford. "Accomodation of misfit between single-crystal films of nickel and copper". In: *Thin Solid Films* 5.3 (1970), pp. 187–198.
[75] EA Owen and D Madoc Jones. "Effect of grain size on the crystal structure of cobalt". In: *Proceedings of the Physical Society. Section B* 67.6 (1954), p. 456.
[76] WL O'brien, T Droubay, and BP Tonner. "Transitions in the direction of magnetism in Ni/Cu (001) ultrathin films and the effects of capping layers". In: *Physical Review B* 54.13 (1996), p. 9297.
[77] *Configured Mini NexGeneration UHV Suitcase MD with Linear/Rotary Feedthrough*. URL: https://www.ferrovac.com/?tool=ProductDescription&product=VSN40M%28CF16%29-0103-MD16-ADCF16TS-RSCPS6OM-TSMDH-0200-0048.
[78] K Kummer et al. "RixsToolBox: software for the analysis of soft X-ray RIXS data acquired with 2D detectors". In: *Journal of synchrotron radiation* 24.2 (2017), pp. 531–536.
[79] Y Song et al. "Spin dynamics in NaFeAs and $NaFe_{0.53}Cu_{0.47}$ As probed by resonant inelastic x-ray scattering". In: *Physical Review B* 103.7 (2021), p. 075112.
[80] K Zhou et al. "Persistent high-energy spin excitations in iron-pnictide superconductors". In: *Nature communications* 4.1 (2013), pp. 1–6.

[81] J Lamsal and W Montfrooij. "Extracting paramagnon excitations from resonant inelastic x-ray scattering experiments". In: *Physical Review B* 93.21 (2016), p. 214513.
[82] GP Purja Pun and Y Mishin. "Embedded-atom potential for hcp and fcc cobalt". In: *Physical Review B* 86.13 (2012), p. 134116.
[83] M Rossi et al. "Experimental determination of momentum-resolved electron-phonon coupling". In: *Physical review letters* 123.2 (2019), p. 027001.
[84] J Rajeswari et al. "Surface spin waves of fcc cobalt films on Cu (100): High-resolution spectra and comparison to theory". In: *Physical Review B* 86.16 (2012), p. 165436.
[85] R Vollmer et al. "Spin-polarized electron energy loss spectroscopy of high energy, large wave vector spin waves in ultrathin fcc Co films on Cu (001)". In: *Physical review letters* 91.14 (2003), p. 147201.
[86] X Liu et al. "Exchange stiffness, magnetization, and spin waves in cubic and hexagonal phases of cobalt". In: *Physical Review B* 53.18 (1996), p. 12166.
[87] M Pajda et al. "Ab initio calculations of exchange interactions, spin-wave stiffness constants, and Curie temperatures of Fe, Co, and Ni". In: *Physical Review B* 64.17 (2001), p. 174402.
[88] *Quanty - a quantum many body script language*. URL: http://www.quanty.org/.
[89] PD Johnson. "Spin polarized photoemission studies of magnetic quantum well states". In: *Journal of magnetism and magnetic materials* 148.1-2 (1995), pp. 167–171.
[90] DJ Huang, PD Johnson, and X Shi. "Quantum-well states and the short period of oscillation in Cu/Co (001) multilayers". In: *Physical Review B* 54.23 (1996), p. 17123.
[91] ZQ Qiu and NV Smith. "Quantum well states and oscillatory magnetic interlayer coupling". In: *Journal of Physics: Condensed Matter* 14.8 (2002), R169.

Appendix A

Proof of the isotropy of spin wave dispersion at long wavelengths

It is useful to generalize the result obtained for the [001] and [0$\sqrt{}$21] axes, showing that the approximatation $E(\mathbf{q}) = D|\mathbf{q}|^2$ is valid in all directions for a fcc lattice. Recalling eq. (2.6):

$$E(\mathbf{q}) = 12JS\left[1 - \frac{1}{12}\sum_{\mathbf{a}}\cos(\mathbf{q}\cdot\mathbf{a})\right] \tag{A.1}$$

We write a generic $\mathbf{q}$ along its components q_x, q_y, q_z. Of course we have:

$$|\mathbf{q}|^2 = q_x^2 + q_y^2 + q_z^2 \tag{A.2}$$

Our first step is to sum all cosine terms. The contribution of the four nearest neighbours in the xy plane is:

$$\begin{aligned}\cos\left(q_x\frac{a}{2} - q_z\frac{a}{2}\right) + \cos\left(q_x\frac{a}{2} + q_z\frac{a}{2}\right) + \\ + \cos\left(-q_x\frac{a}{2} - q_z\frac{a}{2}\right) + \cos\left(-q_x\frac{a}{2} + q_z\frac{a}{2}\right)\end{aligned} \tag{A.3}$$

We do the same also for the yz and zx planes and obtain:

$$\begin{aligned}2\Bigg[\cos\left(\frac{q_x a + q_z a}{2}\right) + \cos\left(\frac{q_x a - q_z a}{2}\right) + \\ + \cos\left(\frac{q_y a + q_x a}{2}\right) + \cos\left(\frac{q_y a - q_x a}{2}\right) + \\ + \cos\left(\frac{q_z a + q_y a}{2}\right) + \cos\left(\frac{q_z a - q_y a}{2}\right)\Bigg]\end{aligned} \tag{A.4}$$

We now expand $cos(x) \approx 1 - x^2/2$ as before:

$$2\Big[6 - \cdot\frac{1}{2}\frac{a^2}{4}[(q_x+q_z)^2+(q_x-q_z)^2+ \\ +(q_y+q_x)^2+(q_y-q_x)^2+ \\ +(q_z+q_y)^2+(q_z-q_y)^2]\Big] \tag{A.5}$$

Which finally reduces to:

$$12 - a^2|\mathbf{q}|^2 \tag{A.6}$$

Plugged into eq. (A.1) gives:

$$E(\mathbf{q}) \approx 12JS\left[1 - \frac{1}{12}\left(12 - a^2|\mathbf{q}|^2\right)\right] = JSa^2|\mathbf{q}|^2 \tag{A.7}$$

Which proves that D does not depend on the direction of spin waves, and can be considered as a general property of the material. With similar arguments the same result can be obtained for bcc and simple cubic lattices. This is equivalent to saying that, at least at low temperatures, anisotropy effects can be fully neglected.

Acknowledgements

This work couldn't have been possible without the help of my family, the guidnance of my supervisor, Giacomo Ghiringhelli, and the whole ID32 team who welcomed me at ESRF for the last six months. My thanks go to all its members: Thomas who taught me practice, Flora who taught me engineering, Kurt who taught me knowledge, Leonardo who taught me hard work, Davide who taught me intuition, Roberto who taught me patience, and finally, Nicholas Brookes who taught me science in its broadest way, day, after week, after month.